TECHNISCHE
UNIVERSITÄT
WIEN
Vienna University of Technology

Diplomarbeit

Quantifying XPS Intensities of Core-Shell Nanoparticles

Ausgeführt am

Institut für Angewandte Physik
der Technischen Universität Wien

unter der Anleitung von

Ao. Univ. Prof. Dr. techn. Wolfgang S. M. Werner

durch

Maksymilian Chudzicki

Mendelssohngasse 7/12,
1220 Wien

_____   _____
Datum   Unterschrift

Kurzfassung

Die Datenbank SESSA (National Institute of Standards and Technology database Simulation of Electron Spectra for Surface Analysis), wurde um die Möglichkeit erweitert Elektronen- und Augerspektren von nanostrukturierten Oberflächen zu simulieren, wie zum Beispiel Inseln, sphärischen Nanopartikeln oder geschichteten Nanopartikeln.

Im Zuge der Arbeit wurde die Schalendicke von Nanopartikeln, bestehend aus einem Kern und einer umhüllenden Schale, mit Hilfe von SESSA bestimmt. Zu diesem Zwecke wurden experimentell bestimmte XPS-Peakintensitäten mit Hilfe von Shards Methode bestimmt und mit SESSA-Simulationen abgeglichen. Es wurde eine sehr gute Übereinstimmung zwischen den experimentell und mit Hilfe der Simulation bestimmten Schichtdicken gefunden in Fällen wo elastische Streuung vernachlässigbar ist. Bei stark streuenden Schichten beträgt die Abweichung der Simulation bis zu 25%.

Mit Hilfe der weiterentwickelten Version von SESSA wurden in weiterer Folge unterschiedliche Systeme von Kern-Schale Nanopartikeln simuliert. Es wurde der Einfluss der Periodizität in der Anordnung der Nanopartikel auf winkelaufgelöste XPS-Peakintensitäten bestimmt. Die untersuchten Systeme reichten von schachbrettartig angeordneten Nanopartikeln über Systeme steigender Unordnung bis hin zu räumlich gänzlich dispersen Anordnungen die eine Schüttung bzw. ein Pulver von Nanopartikeln widerspiegeln. Es wurde gefunden dass sich mit steigender Periodizität die Form der winkelaufgelösten XPS-Spektren ändert, was durch Abschattungseffekte benachbarter Nanopartikel erklärt wird. In weiterer Folge wurde die Validität des single-sphere-Modells bestätigt, das aussagt dass die XPS-Peakintensität eines Pulvers äquivalent zur Peakintensität eines einzelnen Nanopartikels ist. Die Ergebnisse zeigen, dass mit SESSA XPS-Peakintensitäten von Nanopartikeln sehr gut reproduziert werden können, für die korrekte Abbildung des inelastisch gestreuten Untergrunds benötigt es aber einer fortgeschritteneren Modellbildung.

Weiters wurden experimentelle Spektren von funkionalisierten Gold-Nanopartikeln von Techane *et al.* hinsichtlich der relativen Peakintensitäten als auch der Form des inelastisch gestreuten Untergrundes mit SESSA 2.0 abgeglichen und eine zufriedenstellende Übereinstimmung zwischen simulierten und experimentell bestimmtne Spektren erreicht.

Abstract

The functionality of a new version of the National Institute of Standards and Technology database Simulation of Electron Spectra for Surface Analysis (SESSA) has been extended by implementing a new geometry engine. The engine enables users to simulate Auger-electron spectra and X-ray photoelectron spectra for different predefined morphologies (planar, islands, spheres, multi-layer core-shell particles).

We compared shell thicknesses of core-shell nanoparticles derived from core-shell XPS peak intensities using Shard's method, which allows one to estimate shell thicknesses of core-shell nanoparticles, and a series of SESSA simulations for a wide range of nanoparticle dimensions. We obtained very good agreement of the shell thicknesses for cases where elastic scattering within the shell can be neglected, a result that is in accordance with the underlying assumptions of the Shard model. If elastic-scattering effects are important, there can be thickness uncertainties of up to 25 %.

Based on the newly implemented geomtry engine, various systems of core-shell nanoparticles were simulated. It was studied how the angle-resolved core-to-shell photoelectron intensity ratio changed with increasing periodicity of the core-shell nanoparticles. The study entailed single-layered systems of core-shell particles ranging from dispersed structures with a low surface coverage to perfectly aligned arrangements. It was found that with increasing periodiciy of the structure features in the angle-resolved XPS spectra emerge, which can be explained be shadowing effects of adjacent core-shell particles. Also, various powder-like structures of core-shell particles were studied to investigate the validity of the single-sphere model for core-shell particles. The results show that the model correctly reproduces the peak intensities of core-shell particles, but more detailed modeling is needed to describe the inelastic background.

Furthermore, experimental spectra of functionalized gold nanoparticles obtained by Techane *et al.* were analyzed with SESSA 2.0, both with respect to the relevant peak intensities as well as the spectral shape. Good agreement between experiment and theory was found for both cases.

Contents

I.Introduction and Motivation

X-ray photoelectron Spectroscopy (XPS) is a well-established analysis technique commercially available since the 1960's, which - despite its maturity - still draws major interest within the research community. As displayed in figure I.1 there is a steady increase in the number of XPS-related publications published per year since the 1970's [1].

This trend can not be attributed to a single factor, it can be stated however, that XPS is one of the most versatile techniques in surface-analysis as it provides easily accessible qualitative and quantitative information on the investigated sample. One feature that distinguishes XPS from other surface-analysis techniques, such as secondary ion mass spectrometry (SIMS) or Auger-electron spectroscopy (AES) is the ability to simultaneously distinguish the chemical state of an element and conducting quantification (in principle). By virtue of this capability XPS became widely popular in chemical analysis where it is known and utilized under the synonym "ESCA" (electron spectroscopy for chemical analysis). In conjunction with the comparatively simple instru-

Figure I.1.: Updated version of web search results on the number of publications containing the displayed keywords; provided by Cedric Powell through personal communication [1]

mentation and well-known underlying physical principles (i.e., the photoeffect, see chapter 1) it constitutes the most common analysis technique in surface science.

XPS is highly surface-sensitive due to the nature of electron transport processes within solids. Signal electrons, i.e., electrons which are liberated in the course of a photoionization process and are subsequently detected, can only emerge from depths in the order of few multiples of the inelsatic mean free path (IMFP), which is the length an electron will travel at average before experiencing an inelastic scattering event. For typical XPS-experiments with aluminium K_α-sources the IMFP ranges from 1-4 nm, depending on the sample structure and the involved materials. The possiblity to selectively detect electrons emerging from such shallow depths makes XPS very sensitive to morphology changes at this scale and therefore highly suitable for analysis of nanostructured surfaces.

Nanostructured materials (or nanomaterials in short) are a diverse and increasingly important group of materials with novel properties that can be associated to the nanoscaled dimensions of a material. It is well-known that the dispersion, i.e., the ratio of surface to bulk atoms, influences many different physical properties of a given material, such as
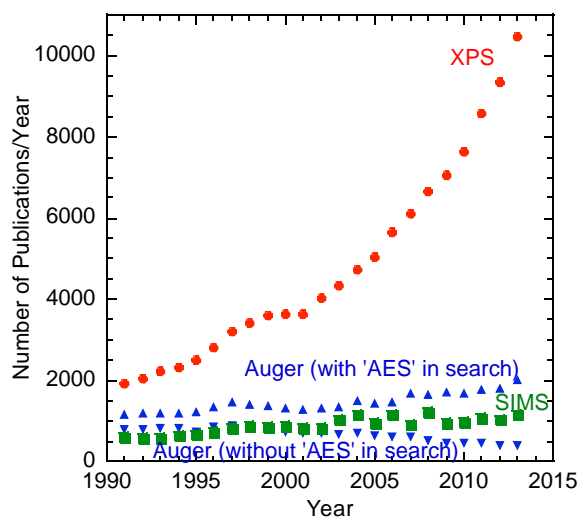
the surface plasmon resonance frequency or superparamagnetic properties. Also, since nanostructures are at the interface between bulk and molecular structures, quantum effects such as quantum confinement can be observed, which is directly related to the dimensions of nanoparticles, as first shown by Ekimov *et al.*on a number of I-VII and II-VI semiconductors [2]. Baer *et al.*studied in a meta-like study the change of various material properties of pure metals and metal oxides as a function size and found that significant changes of the physical and chemical properties occur at the nanoscale [3]. Differently phrased, at the nanoscale thermal, chemical, mechanical and electrostatic energies are in the same order of magnitude providing opportunities for couplig of different types of excitation modes and thus leading to materials with novel properties [3, 4].

However, nanoparticles can exhibit a significant toxic potential to living organisms. Due to the high surface area and the inherent catalytic activity nanoparticles can lead to adverse reactions as was for example the case with asbestos which is the main cause for Asbestosis, a chronic lung disease triggered by inhalation of airborne asbestos fibers [5]. Other types of nanostructures, such as carbon nanotubes were also shown to adversely interact with the human genome and it is therefore of highest priority to subject nanostuctures to diligent toxicity studies. Finke notes that *"Many researchers continue to work with compositionally poorly characterized nanoclusters made by unbalanced reactions leading to nanoclusters of unknown composition."*, which poses a major problem in terms of reproducibility since supposedly equivalent batches of nanoparticles obtained from different manufacturers (or even the same manufacturer) can exhibit strong variations in shape, dimensions and catalytic activity [6]. One can state that the development of new nanostructured materials currently outpaces the characterization capabilities, described as the *nanomaterial characterization bottleneck* [7]. It is therefore necessary to develop rapid, easy and, most importantly, reproducible methods for accurate characterization of nanostructures, so that biological properties can be correctly attributed to the dimensions and structures of the investigated materials [3].

However, extracting structural information from XPS spectra is a non-trivial task requiring in-depth expertise in XPS-modeling and therefore cannot be conducted routinely by XPS operators who are in need of simple algorithms and methods that allow them to obtain reliable results for specific problems within relatively short times. One example of such a method is given by Shard, who derived an equation that allows one to calculate the overlayer-thickness of spherical core-shell (CS) particles of known composition and core dimensions by means of the photoelectron intensity ratio of the core- and shell-electrons [8]. This method (henceforth referenced as *Shard's method*) will be discussed in detail in section 1.1. It should be stressed, however, that when employing methods such as these, it is of highest importance to bear in mind the limitations of the underlying model. Shard's method, for example, performs very well for material systems where elastic-scattering effects within the shell material can be neglected and underestimates the shell thickness otherwise. As will be shown in subsequent chapters elastic-scattering effects are often hard to account for, and therefore many models are based on the straight line approximation (SLA), in which it is assumed that the electron trajectories follow rectilinear paths. Unfortunately many models that are based on the SLA are rendered

useless when materials with high atomic numbers are involved and elastic scattering cannot be disregarded. Furthermore, similar models are only available for the most common nanoparticles, e.g. CS particles or nanotubes. Very often, however, the geometry of the sample differs from such ideal cases for which said models were developed. Thus, a different approach needs to be taken to aid the process of data interpretation.

A very important tool which is highly versatily at the expense of a high level of complexity is the Monte Carlo (MC) method, which enables to simulate an XPS experiment by sampling electron trajectories and tracking their spatial coordinates and the energy losses they experience in the course of the inelastic scattering events. The MC method is a stochastic approach which allows one to simulate electron transport problems without the need to solve analytical transport equations such as the Boltzman equation, by means of which it is nearly impossible to accomodate the complexity of the interaction processes or often complicated spatial boundary conditions. The electron transport process within solids is goverend by elastic and inelastic scattering processes which can be described by means of scattering cross sections, which are statistical quantities describing the total probability of an electron being scattered. The differential cross sections in turn are probability distributions describing the angular and energy dependence of the scattering processes and are therefore critical quantities for electron transport. If an inelastic scattering event occurs, the distribution of energy losses is governed by the differential inverse inelastic mean free path (DIIMFP), a random variable describing the energy loss of an electron in the course of an inelastic scattering event.

With almost abundant computation power of modern computers and sophisticated MC algorithms one is far less limited by the computation time necessary to conduct a simulation than a few years ago. In the last decade various software suites such as SESSA (Simulation of Electron Spectra for Surface Analysis) or QUASES were developed, greatly facilitating the process of simulating XPS experiments and thus enabling a wide range of users, who otherwise would not be able to conduct MC simulations, to develop a better understanding of XPS results through the possiblity to match experimental results with simulations [9–11].

However, the use of third party sofware leads to an inherent lack of flexibility since the software usually can not be extended or customized easily to meet ones specific needs. In the context of nanoparticle analysis it is necessary to define differently shaped nanostructured surfaces, such as spheres, rods, islands or CS particles. Therefore, in order to expand the field of application of XPS simulation software it is inevitable to implement a flexible geometry engine capable of handling the movement of an electron trajectory through a arbitrarily shaped strucutre.

In the present work this need was addressed by implementing the PENGEOM geometry package in SESSA V2.0. The PENGEOM package constitutes of a stand-alone toolbox, distributed within the PENELOPE code system, for defining arbitrary morphologies and tracking of electron trajectories. SESSA is a NIST database containing all physical data needed to perform quantitative interpretation of Auger-electron and X-ray photoelectron spectra. In order to minimize computation times and enable faster processing of batch jobs a highly efficient Monte Carlo code is employed, based on the trajectory-reversal

method by Gries and Werner [12]. In contrast to conventional Monte Carlo codes where electrons are tracked from the source to the detector, in the trajectory-reversal approach electrons are traced in the opposite direction, starting from the detector and following the trajectory back to its point of origin. Thus, all electrons contribute to the signal resulting in significantly decreased simulation times in the range from seconds to several minutes, depending on the specific problem and simulation settings.

In the course of this work a validation of SESSA 2.0's results was conducted using Shard's $T(\mathrm{NP})$ formula to ensure the correctness of the results obtained with the newly implemented geometry engine. Since core-shell particles constitute a particularly imporant class of nanoparticles, angle-resolved XPS spectra was simulated. The investigated structures can be grouped in two classes: single-layered structures and powder-like structures. The former group consisted of arrangements of core-shell particles on a substrate and ranged from highly dispersed structures with a low surface coverage up to regularly aligned structures with the highest possible periodicity. The study of the powder-like structures was conducted to verify the validity of the single-sphere- or powder-assumption which states that the photoelectron intensity ratio of a single sphere is equivalent to the intensity ratio obtained from a bulk powder.

The present work is concluded by a applying SESSA 2.0 to experimental data and reproducing results obtained with SESSA 1.3 and additional modeling which gave very good agreement between the experiment and the simulations.

II.X-ray Photoelectron Spectroscopy

In this chapter the basics of XPS will be explained. This entails the basics of instrumentation as well as the underlying phyiscal principle, i.e., the photoeffect. XPS is an invaluable analysis technique and was developed by Kai Siegbahn at the University of Uppsala and is amongst the most surface-sensitive analysis techniques currently available.

Only few other techniques provide the same or a higher level of surface sensitivity. However, taking into consideration the instrumental simplicity (and thus costs and robustness) and the comparatively easy means of characterization (in principle), it is unsurpassed in the price-to-performance ratio it is providing to surface analysis. Thanks to these facts XPS is by far the most common surface analysis technique used in industrial as well as academic research.

The importance of surface sensitivity becomes apparent in the context of a meanwhile famous phrase coined by the Nobel laureate Herbert Kroemer: *"The interface is the device"* [13]. In essence, all solid materials interact with their environment through interfaces which exhibit very different chemical and physical properties compared to the bulk of the solid. Thus, the physical and chemical properties of interfaces in general and surfaces in particular are of great scientific interest and are subject to intensive research.

Typically, the characteristic length of the interface transition-region is of the order of few nanometers and is therefore accessible through XPS, which is a unique feature of this technique. Moreover, in contrast to other spectroscopy techniques, XPS provides the unique feature of providing chemical state information on the investigated species, which enables one to obtain information on the chemistry of surfaces.

By employing angle-resolved XPS (ARXPS), where the tilt angle of the surface normal relative to the detector is varied, it is possible to discern the oxidation states of oxide film as a function of depth. As further elaborted in section 3, ARXPS experiments pose a very powerful method for depth-profiling of samples, it is however necessary to make assumptions regarding the geometry of the sample which often entail elaborate modeling. In order to facilitate this process, and to develop a deeper understanding of the investigated specimen, simulation software such as SESSA can be employed.

1. The Photoeffect

Electromagnetic (EM) waves can interact with solids in various ways. Depending on the energy regime of the EM radiation different modes of excitation are available. For example, electromagnetic waves with energies of the order of meV can interact with the phononic system of crystals, while EM radiation of higher energy gives rise to plasmon excitations or electronic transitions and, if the energy is sufficient, can lead to liberation of solid-state electrons.

In metals outer-shell electrons can be liberated if the energy of the exciting radiation is higher than the binding energy (relative to the Fermi level) of those loosely bound electrons plus the work function of the material. A schematic illustration of the energy

levels within metals is shown in figure II.1. In this picture the binding energy E_B and the work function ϕ are both given relative to the Fermi level. The binding energy is therefore the energy necessary to elevate an electron to the Fermi level, whereas the work function is the potential that needs to be overcome to liberate an electron form the Fermi level to the vacuum level.

This radiation-induced liberation of electrons from metals is known as the photoelectric effect[1] and constitutes the basis for XPS where low-energy X-rays ($\approx 1.5\,\text{keV}$) are used.

The kinetic energy of a photoelectron (PE) is given by the *photoelectric equation*:

$$E_{\text{kin}}^0 = h \cdot \nu - E_B - \text{e} \cdot \phi \tag{II.1}$$

In this equation E_{kin}^0 stands for the kinetic energy of the electron excited by a photon of energy $h \cdot \nu$. The kinetic energy of the liberated electron is reduced by the binding energy E_B, and the energy $\phi \cdot \text{e}$ needed to elevate the electron to the vacuum level.
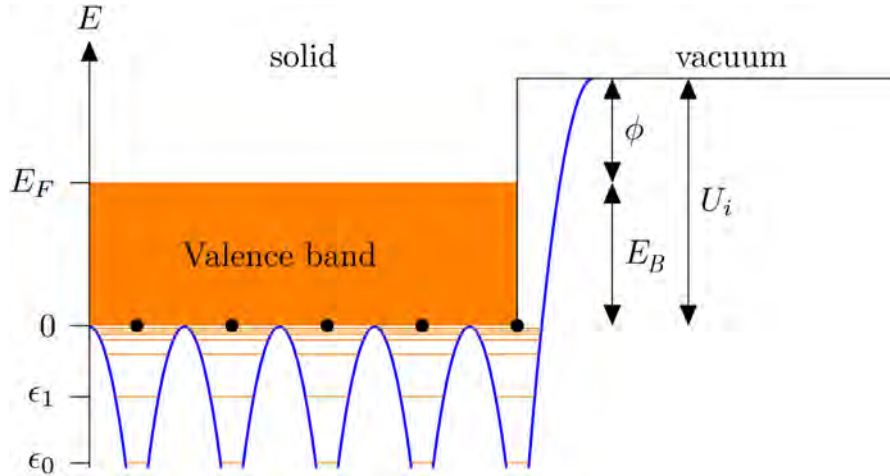

Figure II.1.: Step-barrier model potential at the surface-vacuum interface displaying the potential barrier an electron needs to overcome to leave the solid. ϵ_n corresponds to bound state of the electron; E_F is the Fermi level, and U_i is the inner potential, which is the sum of the binding energy E_B, relative to the Fermi level, and the work function ϕ of the material. Taken from [14]

By means of the photoeffect it is possible to study the electonic structure of an element, for all electrons with binding energies smaller than the energy of the incident radiation will give features in the spectrum. The spectrum of a gold nanoparticle, functionalized with an organic alkanethiol, is shown in figure II.2. It can be seen as a superposition of two groups of electrons: The first group consists of electrons which only participated in elastic scattering events. These electrons give rise to sharp, prominent peaks, which are labeled by the respective orbital they originate from. Peaks from orbitals with an orbital angular momentum quantum number greater than 0 (p-, d- and f-orbitals) are split up

---

[1]First found by Wilhelm Hertz and later explained by Albert Einstein who was awarded the Nobel prize for this achievment.
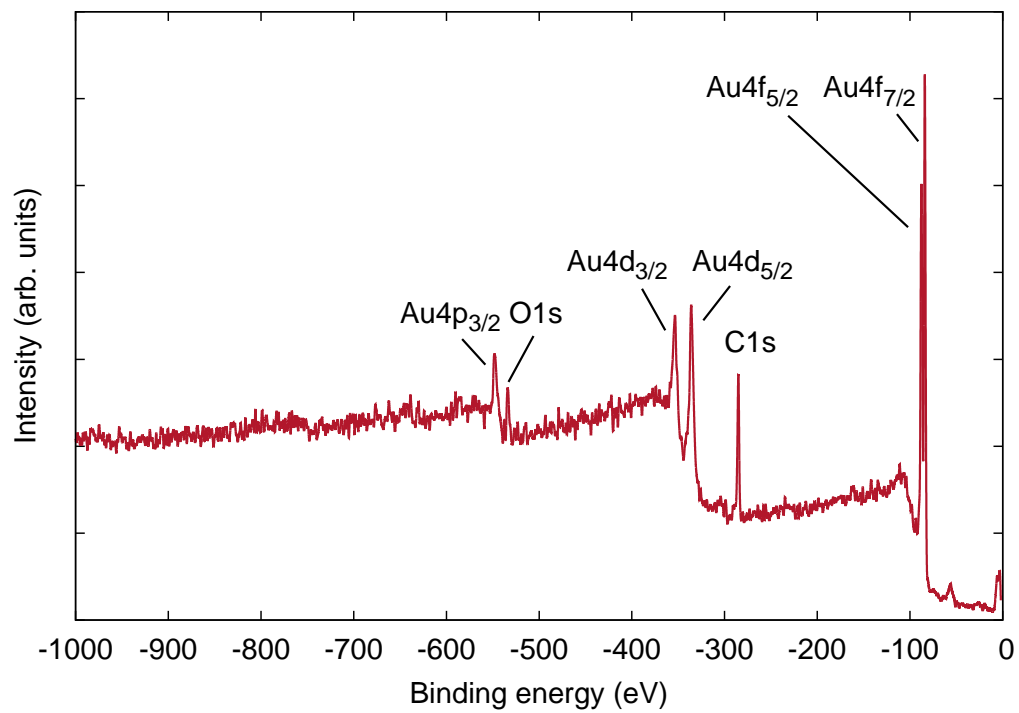
Figure II.2.: XPS spectrum of 14 nm gold nanoparticles functionalized with an organic overshell; provided by Techane *et al.* [15]

into two peaks as a consequence of the interaction of the electron spin with its angular momentum.

The secound group is formed by electrons which participated in one or multiple energy loss events and thus contribute to the continuous background of the spectrum. The form of the inelastic background can provide valuable information on the elemental distribution within a sample since PEs from deeply buried structures will experience more inelastic scattering events than PEs originating from a thin layer just beneath the surface.
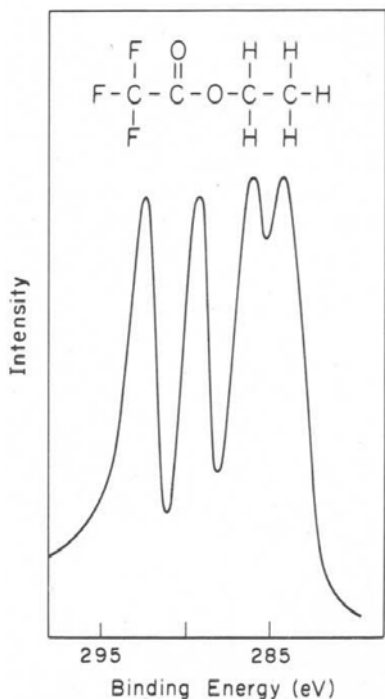

Another important aspect in the context of the photoeffect is the chemical shift. The electronic structure of an element is influenced by its chemical environment (i.e., chemical bonds and oxidation state). Thus, the binding energy of PEs will shift depending on the chemical states of the element, which can be easily discerned by applying peak-fitting methods. One prominent example of chemical shifting is shown in figure II.3 where the C1s spectrum of ethyl trifuloroacetate is shown, which exhibits an extreme shift of the C1s peak due to the highly electronegative trifluoro and carboxyl groups. Each subpeak can be attributed to a different carbon atom within the molecule, resulting in four distinct peaks.

Figure II.3.: C1s spectrum of Ethyl Trifluoroacetate exhibiting extreme shifts of the C1s peak which can be attributed to the Carbon atoms in the molecule [16]

2. XPS Instrumentation

A typical XPS experiment is composed of four main parts that are located in an ultra-high vacuum chamber: an X-ray source, an X-ray monochromator, a sample holder and the detector. High-vacuum or UHV conditions are necessary as samples would be otherwise contaminated within fractions of seconds. Such adsorbates (e.g., adventitious carbon) can heavily impact the results of an experiment due to extreme surface-sensitivity of XPS. Also, UHV ensures that emitted photoelectrons can reach the detection system without being absorbed. In this section a brief descirption of common X-ray sources and electron detectors is given.

2.1. X-ray sources and monochromators

Depending on the specific needs of an experiment, and in particular the desired energy regime of the exciting radiation, different X-ray sources such as synchrotrons, cyclotrons and X-ray lasers are available.

In surface science, however, the most common type of source is an X-ray tube where the

radiation is produced by bombarding a specific anode material with high energy electrons. The electrons are emitted from a thermal source such as a tungsten or lanthanum hexaboride emitter and accelerated throughout the applied field between the emitter and the anode material. Typical acceleration voltages are in the range of several keV and determine the efficiency of the X-ray source, i.e., the number of of X-ray photons generated per impinging electron. Upon impact the electrons knock out inner-shell electrons, leaving behind holes, which are subsequently filled by electrons from outer shells through radiative relaxation.

The main criteria an X-ray source has to meet are a small peak width of the emitted radiation, in order to avoid excessive peak broadening of the spectrum, and the ability to excite intense photoelectron peaks from all elements of the periodic table (except for hydrogen and helium, which are impossible to detect by means of XPS). The most common anode materials are aluminium and magnesium, which give intense K_α-lines of 1486.6 eV and 1253.6 eV, respectively. They are comercially available as twin-anode systems. Such systems enable to seamlessly switch between two different excitation energies and therefore differentiate between Auger and PE transistions, as the former will appear at the same kinetic energies in the spectrum while the latter will change position depending on the employed anode material.

In order to focus the X-ray beam onto the sample and to remove the unwanted background radiation which is produced in the course of electron bombardment of the anode, a monochromator is used. Monochromators produce narrow X-ray lines by using diffraction in a crystal lattice, which is goverened by the well known Bragg equation:

$$n \cdot \lambda = 2 \cdot d \cdot \sin\theta \tag{II.2}$$

in which n stands for the diffraction order, λ for the wavelength of the characteristic X-rays, while d is the crystal lattice spacing and θ the Bragg angle at which constructive intereference occurs. In modern instruments sophisticated setups, such as Rowland circles are used.

The main advantage of using a monochromator is the reduced peak width of the characteristic X-rays which improves the chemical selectivity by narrowing the spectral peaks. Also, depending on the specific monochromator used, it is possible to achieve considerable improvement in lateral resolution of the experiment. State-of-the-art instruments are capable of achieving lateral resolutions in the order of several tens of microns, which is for example used heavily in material science.

2.2. Analyzers and detectors for electron spectroscopy

There are two main types of electron detection systems used for XPS and AES: the cylindrical mirror analyzer (CMA) and the hermispherical mirror sector analyzer (HMA). Both types excel at different aspects of electron detection. For example, HMAs provide better energy resolution while CMAs have generally higher sensitivity [17]. For XPS, the most important factor in electron detection is the spectal resolution. Thus, HMAs constitute the most common detector type in XPS and will be described in this section.

Hemispherical analyzers

A HMA consists of two concentrically aligned hemispherical electrodes, a lens system placed before the HMA and a electron detector at the end. The basic design of a HMA is shown in figure II.4. Different voltages are applied to each hemisphere, such that there is
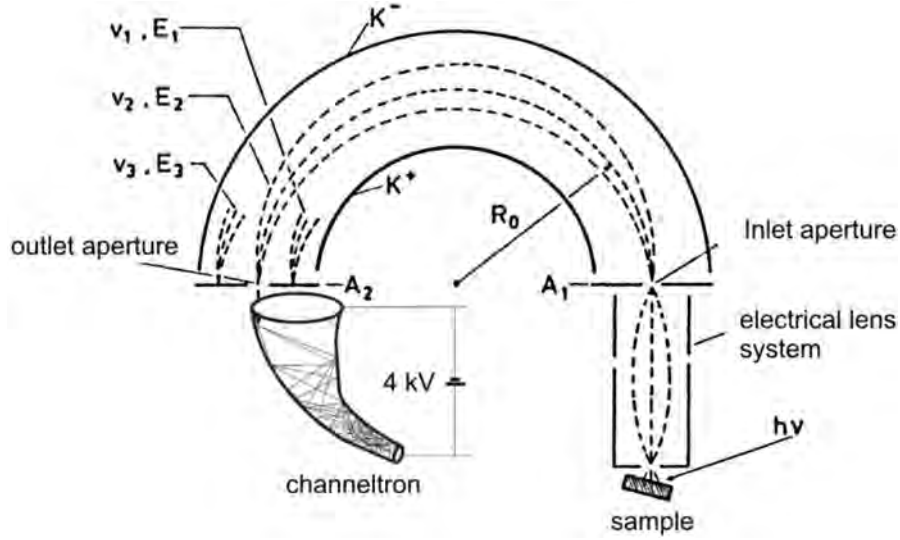

Figure II.4.: Schematic design of a hemispherical analyzer with a channeltron. Taken from [18]

a resulting electric field within the void area between both electrodes. Electrons ejected from the sample are injected into the HMA after passing a series of lenses which are placed before the entry slit of the analyzer.

The transfer lens system serves different purposes: First, it allows to position the HMA at a distance from the sample, so that other parts of the spectrometer can be placed closer to the sample. Also, the lens system determines the analyzer acceptance angle as well as the sampling area of electrons. Most importantly, the lens system attenuates the incoming electrons so that they can be analzed by the HMA with sufficient and constant resolution. In a typical XPS experiment with an aluminium K_α source, the photoelectrons emitted from the sample have kinetic energies ranging from tens of eVs up to approximately $1\,\mathrm{keV}$. However, only electrons of energy, the so-called pass energy

$$E = e\Delta V \left(\frac{R_1 R_2}{R_2^2 - R_1^2} \right)$$

can reach the detector. In this equation e is the elementary charge of the electron, ΔV is the potential difference between the hemispheres, and R_1 and R_2 are the radii of the inner and outer hemispheres, respectively. Since the radii of the hemispheres are constant, the equation can be rewritten:

$$E = ke\Delta V \tag{II.3}$$

where k is the spectrometer constant and depends on the spectrometer design. If the kinetic energy of an electron is significantly higher than given by this equation, it will follow a path that is larger than the mean radius of the two hemispheres and it will not reach the detection area. Vice versa, if the energy is too low, the electron will impinge the inner hemisphere instead of getting detected. Thus, only electrons in a narrow energy region around E, the pass energy, will reach the detector.

HMAs can be operated in two different modes: constant analyzer energy (CAE) and constant retard ratio (CRR). In the CAE mode electrons are accelerated or retarded by the lens system attached to the HMA to the predefined pass energy of the HMA. To record a electron spectrum the retardation energy is scanned, so that electrons of a different primary energy are accelerated or retarded to the pass energy. The resolution of the HMA is affected by the pass energy, thus, for a given pass energy, the absolute resolution (in eV) is constant across the entire width of a spectrum. Depending on the goal of the analysis (i.e., survey spectrum of estimation of chemical state information), the pass energy will be set accordingly.

In the CRR mode the the electrons are slowed down by the lens system by a constant ratio and the pass energy is adopted accordingly, as shown in equation II.4

$$\text{Pass energy} = \frac{\text{Kinetic energy}}{\text{Retard ratio}} \tag{II.4}$$

The resolution is constant throughout the width of the spectrum and is inversely proportional to the retard ratio:

$$\text{Resolution} \approx \frac{2}{\text{Retard ratio}}\% \tag{II.5}$$

The CRR mode is often used for Auger-electron spectroscopy as the transmission increases with increasing kinetic energy as it suppresses the relatively high electron yields at low kinetic energies. In XPS, however, the CAE mode is preferred as the transmission and resolution (in eV) remain constant throughout the whole spectrum, thus making quantification easier.

Electron detectors

For detection of electrons that passed through the HMA, electron multipliers are used. Two main types are currently employed in XPS spectrometers: channel electron multipliers (channeltrons) and channel plates.

Channeltrons Channeltrons are spiral-shaped tubes coated with a material with a high secondary-electron yield. Thus, when struck by an electron of some energy higher than some material-specific threshold energy, it will emit many secondary electrons. These secondary electrons will be accelerated further into the tube by means of the applied potential difference and result in a cascade of electrons which will be create a current at the end of the tube that is proportional to the number of electrons entering the

channeltron. The gain of the channeltron depends on the applied voltage and obtains typical values of approximately 10^8. The detection efficiency of a channeltron depends on the applied voltage. With increasing voltage, however, the detection efficiency reaches a plateau, which is also the typical operation point of the channeltron.

Channel plates A channel plate is a plate with regularly aligned holes in it, where each hole serves the same purpose as a channeltron. Due to the design the gain as well as the maximum countrates are smaller than in the case of individual channeltrons. However, channel plates can be used to detect data in two dimensions, which can be used in a variety of setups. For example, by using channel plates it is possible to record position-dependent photoelectron images or simultaneously record angle- and energy resolved XPS spectra.

3.   Quantitative X-ray Photoelectron Spectroscopy

The analysis of XPS spectra can range from a basic qualitative determination of the elemental composition to a sophisticated quantitative analysis based on advanced modeling, including chemical analysis and spatial distribution of elements. This section gives a brief overview over the most important aspects of quantification of XPS spectra based Watts' book on the surface analysis by XPS and AES [17].

3.1. Depth of analysis

The surface sensitivity of XPS is inherently related to the processes governing electron transport in solids. As PEs are liberated in the course of the photoionization process they propagate through the material and interact with the solid through scattering processes with the ionic and electronic subsystems of the material. Since the masses of the PEs and the nuclei forming the ionic subsystem differ by several orders of magnitude, scattering with the Coulomb potential of the nuclei gives rise to negligible energy transfers of the order of tens of meV, and considerable momentum transfer. Thus, the electron is significantly deflected from its original trajectory.

On the other hand, scattering of PEs with the electronic subsystem leads to significant energy transfers with minimal momentum transfer, thus leaving the direction of the electron unaffected.

The characteristic path lengths an electron travels before experiencing either interaction are known as the inelastic and elastic mean free paths, respectively (IMFP and EMFP). Figure II.5 shows both quantities for a wide energy range for gold and aluminium.

The escape depth, and thus depth of analysis of XPS can be directly attributed to these quantities, which are combined in the effective attenuation length (EAL). While in a first approximation the EAL can be seen as equivalent to the IMFP, this relationshop only holds for light elements where elastic-scattering effects can be neglected. This relationship is represented by the difference between the IMFP and the EMFP for aluminium and gold, as shown in figure II.5, where in the former case both quantities are almost identical,
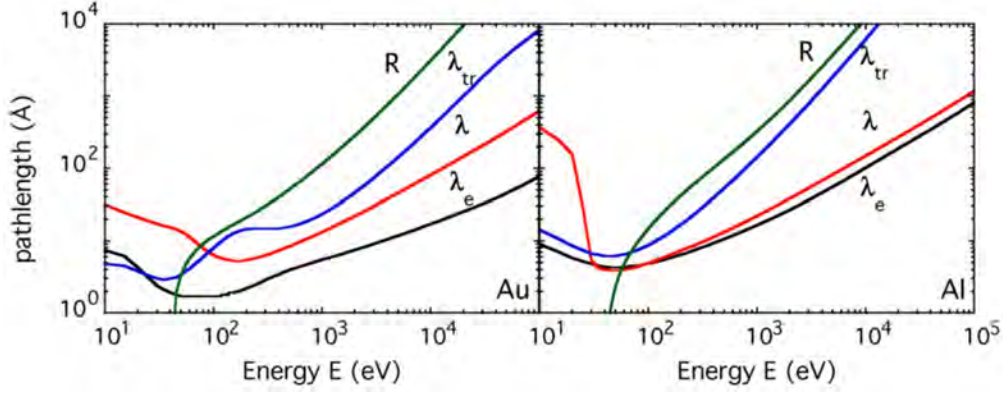
Figure II.5.: Characteristic path lengths for electron transport for gold and aluminium as a function of energy. λ: IMFP; λ_e: EMFP; λ_tr: transport mean free path; R: linear range; figure taken from [19]

while in the latter case the EMFP is significantly smaller. Due to the increased scattering potential of elements with a high atomic number Z, the resulting electron trajectories do not follow near-rectilinear paths anymore, which needs to be accounted for by using the EAL instead of the IMFP for quantification purposes. [20]

For a homogenous, semi-infinite sample, the intensity of electrons emitted from all depths greater than d is given by the Lamber-Beer relationship:

$$I = I_0 \cdot \exp\left(-\frac{d}{\lambda_\mathrm{EAL} \cos\theta}\right) \tag{II.6}$$

where I_0 is the total photoelectron-intensity emitted from the specimen, λ_EAL is the EAL and θ is the emission angle realtive to the surface normal. Varying the emission angle allows one to selectively detect portions of electrons originating from shallower depths and thus conduct non-destructive depth profiling. This possibility is utilized in angle-resolves XPS (ARXPS), a technique where the electron emission angle to the detector is varied by tilting the sample[2]. The relative electron emission intensity as a function of emission angle is shown in figure II.6, where multiples of λ_EAL are highlighted. Depending on the emission angle, the major contributions to the signal originate from different depth ranges, thus allowing for a depth-dependent analysis of the specimen. At an emission angle of $\theta = 0°$ 95% of the signal originates from a depth of $\approx 3\,\lambda$ while the same intensity ratio is obtained from a depth of less than $\approx 1.5\,\lambda$ at an emission angle of $\theta = 60°$. Due to the angular dependence of the signal intensity, the emission depth can be more correctly written as $\approx 3\,\lambda \cdot \cos\theta$.

---

[2]Some modern instruments are equiped with wide-angle analysers which enable to record ARXPS spectra without the need to mechanically tilt the sample
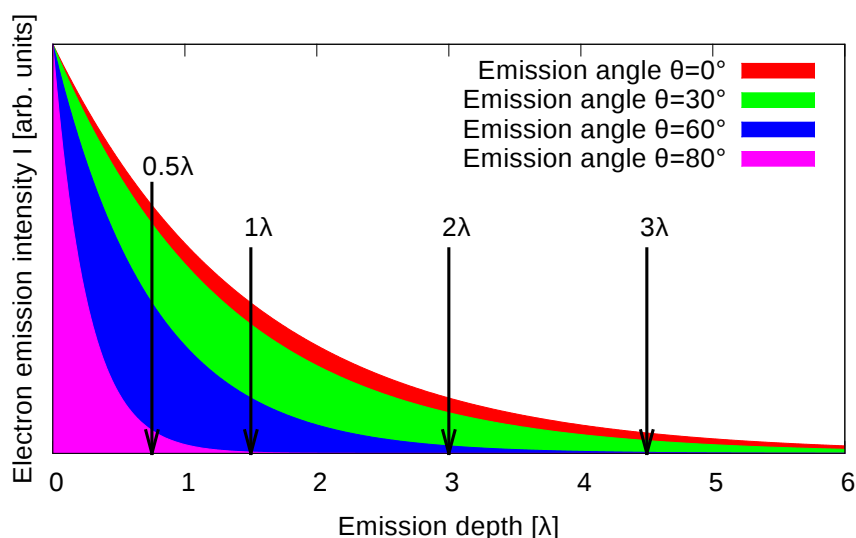
Figure II.6.: Relative electron intensity as a function of depth for a EAL of $\lambda_{\mathrm{EAL}} = 1.5\,\mathrm{nm}$

3.2. Factors affecting the quantification of XPS spectra

Even in the simplest case of a semi-infinite sample with a homogenous elemental distribution (like a slab of TiO_2), a number of factors have to be considered in order to conduct a qualitative assessment of the elemental composition. These can be grouped into sample-related and spectrometer-related factors [17]:

Sample-related factors The cross-section (CS) for emission of electrons due to the photoionization by the incoming radiation depends upon a range of parameters, such as the element under investigation, the orbital from which the electron is ejected, the energy of the exciting radiation and the angle between the analyzer and the source. For XPS, the cross-section for emission of a PE increases for a given series or core levels (i.e., 1s, 2p, etc.). In AES, the probability for emission of an Auger-electron depends upon the atomic number in a more complex manner, however, in general, the Auger-electron yield decreases with the atomic number as radiative relaxation becomes more probable.

Moreover, as shown in figure II.5, the escape depth of the emitted electrons is a function of the kinetic energy and, most importantly, the material they are passing through. That means, PEs with higher kinetic energy can escape from larger depths than electrons with smaller kinetic energy.

In practice however, perfectly homogenous, semi-infinite samples are rarely encountered. Therefore, one needs to account for the impact of interfaces, contamination layers, shadowing effect, surface roughness etc.

Spectrometer-related factors If a sample was to be measured in two different XPS instruments, the resulting spectra would not be identical, as both instruments exhibit different transmission functions. The transmission function determines the portion of

electrons transmitted through the electron optics system from the sample to the detector, as well as the detector efficiency itself. If not compensated or shielded, stray magnetic fields can influence both parameters. Typically spectrometer-related factors are accounted for by the manufacturer of the instrument and corrections are implemented in the analysis software.

Sample-related factors affecting the quantification of electron spectra can be condensed into relative sensitivity factors (RSF). For the peak intensity of a homogenous sample one can write:

$$I^\infty = J \, \rho \, \sigma \, K \int_0^\infty \exp\left(-\frac{z}{\lambda_{\mathrm{EAL}}}\right) \mathrm{d}z \tag{II.7}$$

$$= J \, \rho \, \sigma \, K \, \lambda_{\mathrm{EAL}} \tag{II.8}$$

where J stands for the absolute photon flux, ρ is the atomic density of species, σ is the cross-section for electron emission, K is a term including all instrumental factors (such as the transmission function, detector efficiency, the detector acceptance angle, etc.) and λ_{EAL} is the EAL. The last three factors combined together form the RSF.

RSFs are correction factors, which provide means to convert peak intensities into atomic concentrations and are therefore critical paramters for quantification in XPS. RSFs can be calculated theoretically, which is known as the *first principle approach*. In most cases, however, the RSFs are determined experimentally and tabulated for a specific instrumental setup. They can be determined by simulating or measuring the intensity of the respective PE peaks originating from semi-infinite samples of all elements in the periodic system, which allows for subsequent quantification of samples with a homogenous elemental distribution.

Once the PE peak intensities are extracted from the spectrum by substracting a linear background or by means of a more sophisticated method, such as Tougaard's background substraction, calculating the atomic percentage of some species A within the sample can be calculated as follows:

$$[\mathrm{A}] \, \mathrm{atomic}\% = \frac{\dfrac{I_{\mathrm{A}}}{\mathrm{RSF}_{\mathrm{A}}}}{\sum \dfrac{I_i}{\mathrm{RSF}}} \tag{II.9}$$

where the index i indicates a summation over all elements in the spectrum. Equation II.9 presumes a homogenously distributed elemental composition of the sample, which can be tested by conducting an ARXPS experiment. If the composition is not independent of the surface normal angle a more rigorous analysis using a suitable model needs to be conducted. The following section shows how the thickness of a overlayer-substrate system consisting of a metal and its oxide can be estimated using the Lambert-Beer realtionship.

4. Compositional depth profiling of a overlayer-substrate system

Overlayer-substrate systems are typical systems for anaylsis with XPS. For example, the thicknesses of technological coatings are typically overlayer-substrate system with overlayer-thicknesses in the range of nanometers and a routinely invstigated with XPS [21].

However, in contrast to homogenous systems, determining the overlayer-thickness based on the peak intensity ratio of an overlayer-substrate system is more difficult and usually requires employing several approximations in order to obtain a simple analytical approximation.

Figure II.7 displays an overlayer-substrate system together with a graphical representation of the Lambert-Beer relationship and the portions of the exponential function which contribute to the intensity of each material. This representation, however, only holds if
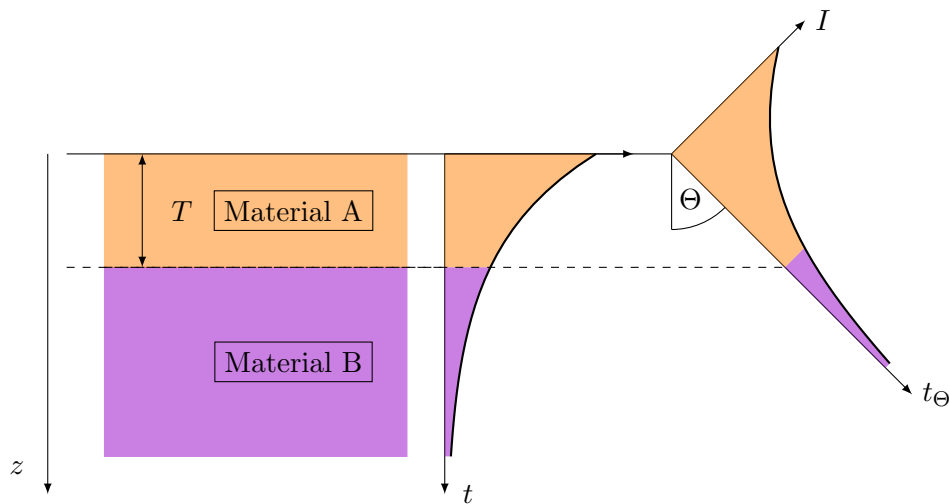
Figure II.7.: Visualization of the established model for layered specimens for two different emission angles Θ. From the detectors point of view the overlayer thickness T increases with the emission angle Θ, which results in a higher fraction of detected overlayer-electrons in direction t_Θ than t.

the following assumptions are met:

- The electron trajectories follow rectilinear paths, which is known as the straight line approximation (SLA) and is a reasonable assumption for systems of low atomic number Z.

- The EALs of the overlayers and substrates are equivalent. This is a common approximation for systems comprised of a metal and its oxide which becomes progressively inaccurate with increasing difference in atomic numbers between the overlayer and substrate materials.

- The acceptance angle of the analyzer is infinitely small, which is an idealization of a real analyzer which always has a finite opening angle (a typical value for the opening angle of a hemispherical analyzer is $12°$).

By imposing these assumptions, the PE intensity of the overlayer material (denoted by the subscript "A") is given by integrating equation II.6 between 0 and d and substituting the expression II.6:

$$I_A = J \rho \sigma K \int_d^0 \exp\left(\frac{-z}{\lambda_{A,A} \cos\theta}\right) \mathrm{d}z \tag{II.10}$$

$$= J \rho \sigma K \lambda_{A,A} \cos\theta \left[1 - \exp\left(-\frac{d}{\lambda_{A,A} \cos\theta}\right)\right] \tag{II.11}$$

$$= I_A^\infty \cos\theta \left[1 - \exp\left(-\frac{d}{\lambda_{A,A} \cos\theta}\right)\right] \tag{II.12}$$

with $\lambda_{A,A}$ being the IMFP of material A within itself. Accordingly, the substrate intensity at depth d is given by the integration from d to ∞. The intensity originating from the substrate at depth d is I_B^∞ and is attenuated exponentially as the PEs propagate through the overlayer. Thus, the intensity is given by:

$$I_B = I_B^\infty \cos\theta \exp\left(-\frac{d}{\lambda_{B,A} \cos\theta}\right) \tag{II.13}$$

The characteristic length of attenuation is $\lambda_{B,A}$, i.e., the attenuation length of PEs originating from the substrate within the overlayer-material. The PE intensity ratio R is therefore given by:

$$\frac{I_A}{I_B} = R = R^\infty \frac{1 - \exp\left(-\frac{d}{\lambda_{A,A} \cos\theta}\right)}{\exp\left(-\frac{d}{\lambda_{B,A} \cos\theta}\right)} \tag{II.14}$$

where $R^\infty = I_A^\infty / I_B^\infty$, i.e., the intensity ratio of the pure substrate- and overlayer-materials, respectively, which can be obtained either by simulation or measurement. If the material system consists of a metal and its oxide (e.g. silicon and silicon oxide) and the overlayer is thin compared to the characteristic lengths, then the approximation $\lambda_{A,A} = \lambda_{B,A} = \lambda_A$ is applicable and equation II.14 can be rearranged to:

$$R = R^\infty \left[\exp\left(\frac{d}{\lambda_A \cos\theta}\right) - 1\right] \tag{II.15}$$

$$= \ln\left[1 + \frac{R}{R^\infty}\right] = \frac{d}{\lambda_A \cos\theta} \tag{II.16}$$

Measuring XPS spectra at various emission angles θ and plotting the left hand side of equation II.16 as a function of $1/\cos\theta$ should yield a straight line with slope d/λ_A which

allows to estimate the overlayer thickness d in units of λ_A.

If the material system does not consist of a a metal-metal oxide pair, and the energies and MFPs therefore differ significantly, equation II.14 needs to be used to estimate the overlayer thickness, which requires additional knownledge of the mean free paths of the substrate PEs within the overlayer-material. Furthermore, both equations II.14 and II.15 are only valid up to emission angles of approximately 60°. Beyond that value linearity breaks down, as a result of elastic-scattering effects. Elastic collisions can lead to underestimation of the overlayer thickness if electrons originating from the metal are scattered into the detection cone and thus contributing to the substrate signal leading to a underestimation of the overlayer thickness.

To correctly account for elastic-scattering effects analytically, it is necessary to employ either correction factors, which are element-specific and applicable to layered samples only [22], or to solve the Boltzman transport equation, which is a laborious task and therefore cannot be done on a routine basis and without special expertise.

However, the problem can be modeled by means of a MC simulation, which simulates discrete electron trajectories. The elastic and inelastic interactions with the solid are accounted for by simulating scattering events based on tabulated cross section data and thus circumventing the necessity to solve an analytical expression which might be hard or impossible to model and solve. With the presently available computation power MC simulations can be conducted on a routine basis and thanks to ergonomic user interfaces can be performed by users with basic knowledge in the field of XPS. A brief introduction into MC simulations is given in the subsequent sections.

Figure II.8 shows a plot of $\ln\left[1 + {R}/{R^\infty}\right]$ as a function of ${d}/{\lambda \cos\theta}$, as seen in equation II.16, displaying experimental data and SESSA simulations conducted with elastic scattering (solid line) and under the SLA (dashed lines) [10, 23]. It can be seen that the straight line approximation gives reasonable agreement with experimental data up to values of $\approx {1}/{\cos 60°} = 2$, which is due to the increasing impact of elastic-scattering effects at oblique angles.

Furthermore the equations derived in this chapter are valid for infinitely small detector acceptance angles and rectilinear electron trajectories. These assumptions are never met in reality and in order to account for both, Monte Carlo simulations can be employed to study the effects arising from the real setup. For example, the use of wide-angle lenses, which allow to record ARXPS spectra simultaneously without the need to tilt the sample implies that the analzer-source angle is not constant anymore, and thus the anisotropy of the photoelectron emission cross section needs to be considered for quantification purposes. Figure II.9 shows experimental and simulation results of the aluminium 2s and 2p PE intensity ratio as a function of the analyzer polar angle [10, 24]. The simulations were carried out based on the SLA (solid line), the so-called transport approximation (dashed line), and using relativistic Mott cross sections for elastic scattering. The analyzer opening angle was set to 6°.

The simulations based on the SLA yield a finite value for an analyzer polar angle of 0°, despite the fact that the photoemission cross section is 0 at this angle for the aluminium 2s orbitals, which is due to the finite analyzer acceptance angle. The agreement with
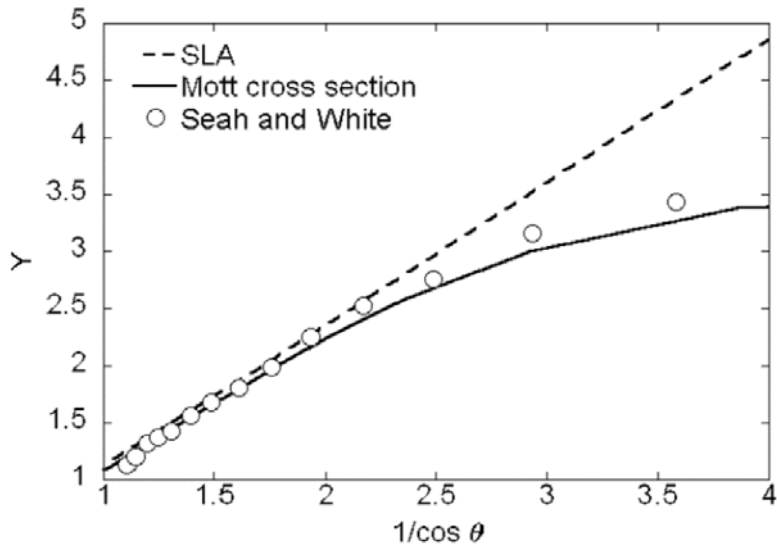
Figure II.8.: Plot of $Y = \ln\left[1 + {}^R/R^\infty\right] l$ as a function ${}^1/\cos\theta$ for a Si/SiO$_2$ material system. The open symbols correspond to experimental data while the solid and dashed lines show SESSA simulation results obtained with elastic scattering and the SLA, respectively [10, 23].
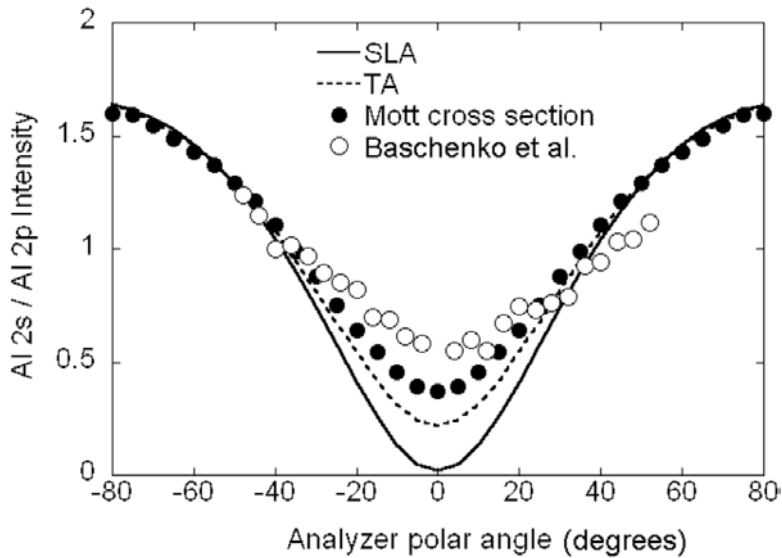
Figure II.9.: PE intensity ratio of the aluminium 2s and 2p orbitals as a function of the polar emission angle. The open circles represent experimental data by Baschenko *et al.* The remaining lines represent SESSA simulations obtained with the SLA, the transport approximation and Mott cross sections, respectively. The experimental data was recorded in transmission while the simulations were carried out in reflectance with a varying analzyer polar angle [10, 24].

experimental data, however, is insufficient, which is due to the assumption of rectilinear electron trajectories. Simulations with the TA or Mott cross sections give much better agreement with the experiment and thus show the importance of accounting for elastic scattering, which can be facilitated by using simulation software such as SESSA.

4.1. XPS in Nanoanalysis

In this chapter it is demonstrated how the spatial distribution of phases within a specimen can affect the inelastic background in an electron spectrum and subsequently it is highlighted how indispensable simulation tools are for the quantification of nanostructured surfaces.

As described in the preceding sections, XPS is a highly surface-sensitive technique which allows one to study the chemistry and structure of materials at the nanometer-scale. For quantification of structures beyond the simplest case of a homogenous phase with a given stochiometry, various algorithms for quantification of nanostructures have been developed throughout the years. However, in most cases, these models were developed for simple and well-defined nanostructures, such as stratified layers or islands on a substrate, and are based on the premise of preexisting knowledge of the structure at hand. Thus, one of the limiting factors in quantification of XPS spectra is how accurately the geometry of the investigated structure is known and how well the model used for quantification reproduces the structure. On the other hand, the accuracy of the result is limited by the knowledge of other factors, such as the photoionization cross sections, IMFPs, EMFPs, surface roughness (if applicable), the influence of elastic-scattering effects or the transmission function.

Presently, XPS is increasingly utilized to study more advanced nanostructures, such as spherical core-shell particles, islands, or functionalized nanotubes. Such structures may exhibit phases with inhomogenous elemental distributions or radially varying atomic densities, which poses a major challenge for modeling. An example of such a structure is given in the scope of this work in chapter 4.2, where XPS spectra of alkanethiol SAMs on gold nanoparticles are investigated. Due to the spreading-out of those discrete chains, the functionalized nanoparticles exhibit a radial decrase in atomic density within the shell, and only after accounting for this decrease it is possible to obtain a satisfactory agreement between the measured and simulated spectra, and, subsequently, the shell thickness of the overlayer.

Traditional XPS is based on the interpretation of peak intensities, meaning that peak areas originating from two distinct elements present in different phases of a system can be used to calculate a morphological feature of the system (e.g., an overlayer thicknes). Thus, in the past many efforts were made to develop methods for background substraction so that peak intensity ratios could be extracted from measured spectra.

However, in many cases a thorough study of the inelastic background provides valuable information on the investigated morphology, as illustrated in figure II.10. Figure II.10 shows how differently distributed phases of copper in gold can affect the inelastic background of the respective normalized XPS spectra [25]. Obviously, if one would quantify these spectra on the basis of the peak intensities without a deeper knowledge of the
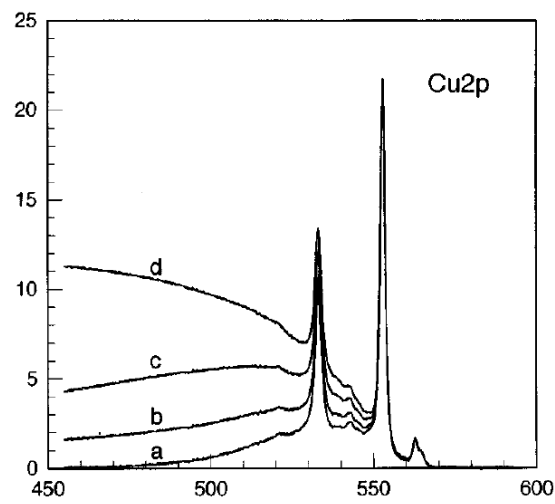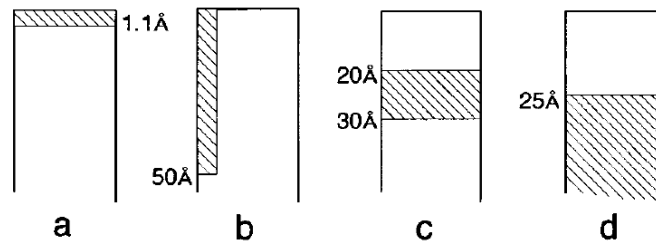
Figure II.10.: Normalized XPS intensity of different copper distributions in a gold matrix giving the same peak intensity with different inelastic background shapes [26]

underlying structure, huge quantification errors would be made, which in case of more advanced structures would be further amplified. By taking into account the shape of the inelastic background accompanying the Cu2p-peak, a deeper understanding of the spatial distribution of the copper-phase can be obtained, which was studied by Tougaard *et al.* in a number of seminal works [25, 27–32]. In essence, the intensity of a given spectral region strongly correlates with the depth at which a photoelectron was generated. This can be easily seen by comparing the cases *a* and *d* in figure II.10, where the former has a very weak background, indicating that the photoelectrons originate from a shallow depth, while in the latter case the background constitutes the dominant feature of the presented spectrum and therefore the Cu2p photoelectrons must originate from deeper buried regions.

In many cases it is necessary to refrain from merely relying on the peak intensity ratios, especially if no models are present which allow for direct translation of peak intensity ratios into distinct features of the investigated morphology. If no models are present, and due to the variability of modern nanostructures (which vary widely in shape, size, coverage, etc.), it is necessary to employ simulation tools, such as SESSA V2.0, which allow to gain information on the investigated structure by matching simulated and measured XPS spectra. By varying various aspects of the simulation, or, in this context, aspects of the mophology, one can try to bring both spectra to agreement, indicating that the measured spectrum originates from the corresponding morphology.

However, even with this rather general approach it is not always guaranteed that all features of a structure can be successfully represented. For example, gold nanoparticles are seldomly perfectly spherical, however, aside from normal fluctuations in diameter and shape, they are in fact comprised of (100) and (111) terraces, which becomes a increasingly important factor with decreasing size of the particles and needs to be considered in simulations of very small nanoparticles [33].

For simulation of core-shell particles the so-called powder-assumption is often applied, which implies that the photoelectron peak intensities originating from a single core-shell particle is equivalent to the peak intensity ratio obtained from a bulk power. However, the main shortcoming of this model is the fact that while it correctly reproduces the peak intensity ratio, it fails to correctly reproduce the background shape, and simulation software such as SESSA needs to be employed to reproduce the correct shape of the background.

5. Monte Carlo Simulation of X-ray Photoelectron Intensities

This chapter aims to summarize the theory of electron-solid interactions and quantitative analysis of eletron spectra based on the partial intensity approach and the Landau-Goudard-Saunderson loss function. Based on this theoretical foundation, a brief description of the Monte Carlo algorithm employed in SESSA is given.

The partial intensity approach stems from the fact that a liberated PE can experience a varying number of elastic and inelastic collisions as it escapes the solid. Depending on

the number n of inelastic collisions the PEs will contribute to the elastic peak ($n = 0$) or the inelastic background ($n = 1, 2, 3, \dots$). Thus, a full PE spectrum can be viewed as a superposition of elastically and inelastically scattered groups of electrons which can be classified by the number of collisions they participated in. Since elastic scattering only contributes to momentum relaxation but not energy dissipation, a PE spectrum can be grouped according to the number of inelastic collisions, where electrons which were scattered $n = 0, 1, 2, \dots$ times correspond to the zero, first, second,... order partial intensity. In the following section a qualitative derivation of the partial intensities is given.

5.1. Electron-solid interaction characteristics

Electrons can interact with the ionic and electronic subsystems of the solids they propagate through. Both interactions are essentially different in terms of momentum relaxation and energy transfer. A collision between an impinging electron and a nucleus will lead to negligible energy transfers due to the huge mass difference of the interaction partners, but will give rise to considerable momentum transfer, which manifests itself in deflections from the initial trajectory path. These deflections may assume values of the order of π for a considerable portion of all scattering events.

On the other hand, inelastic collisions with the solid state electrons lead to considerable energy transfers of the order of $10\,\text{eV}$, however, the momentum transfers, and thus the changes in the direction of motion, are negligible. Therefore, the description of electron scattering processes can be separated into elastic and inelastic processes which can be described independently.

Elastic scattering

When an electron undergoes an elastic collision with a nucleus its energy prior to and after the collision is virtually unchanged. However, in the vicinity of the nucleus' potential well, the energy of the electron and therefore its wavelength vary considerably, which results in a phaseshift of the emerging wave. The scattering of a plane wave can be expressed by the following wave function, which is the sum of an incoming plane wave e^{ikz} and a outgoing spherical wave e^{ikr}/r:

$$\psi(\vec{x}) \sim e^{ikz} + f(\theta)\frac{e^{ikr}}{r} \tag{II.17}$$

where $f(\theta)$ is the scattering amplitude. It is closely related to the differential cross section by

$$\frac{\text{d}\sigma_{\text{e}}}{\text{d}\Omega}(\theta) = |f(\theta)|^2 \tag{II.18}$$

with the subscript "e" denoting elastic scattering. If the potential is spherically symmetric, as in the case of a Coulomb potential, equation II.17 can be expanded in spherical

harmonics of different angular momentum l. The scattering amplitude is then given by:

$$f(\theta) = \frac{1}{2ik} \sum_{l=0}^{\infty} (2l+1)(e^{2i\delta_l} - 1) P_l(\cos\theta) \tag{II.19}$$

with l being the angular momentum quantum number, k the electron wave vector and $P_l(\cos\theta)$ the respective Legendre polynomial. By calculating the phase shift δ_l of each partial wave by solving Schrödinger's or Dirac's equations one can calculate the scattering amplitude and the cross section for elastic scattering using equation (II.18).
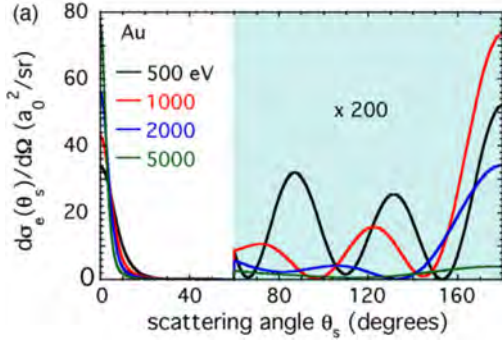

Figure II.11.: Differential elastic cross section for gold for different electron energies

Figure II.11 shows the calculated differential elastic cross section (DECS) of electrons of different energies in gold. The DECS corresponds to the distribution of polar scattering angles in individual scattering events. It exhibits an oscillatory behaviour due to interference effects of the incoming and outgoing waves which increases with the atomic number of the target and decreasing electron energy. For very light elements and high energies the DECS exactly coincides with the classical Rutherford cross section which can be derived from classical mechanics. Also, the DECS always exhibits a pronounced forward-scattering peak. The width of this peak relates to the average length of the path traveled by an electron before experiencing the next elastic collision, also known as the elastic mean free path (EMFP). The EMFP can be obtained by integrating the DECS over the unit sphere and taking into account the atomic density N_a:

$$\lambda_e^{-1} = N_a \int_{4\pi} \frac{d\sigma_e}{d\Omega}(\Omega)\, d\Omega \tag{II.20}$$

By introducing the weighting factor $(1 - \cos\theta)$ into equation II.20 one can calculate the transport mean free path (TRMFP) which corresponds to the momentum transfer along the initial direction since the weighting factor emphasizes large scattering angles. Differently phrased, it is the average distance an electron travels before the next large-angle scattering event, which significantly contributes to the momentum-relaxation process.

$$\lambda_{tr}^{-1} = N_a \int_{4\pi} (1 - \cos\theta_s) \frac{d\sigma_e}{d\Omega}(\Omega)\, d\Omega \tag{II.21}$$

Inelastic scattering

In contrast to elastic scattering and the DECS, which is an atomic quantity derived from the interaction of an electron impinging on a discrete target, inelastic scattering

is governed by a many-body interaction of the electron with the surrouding electronic subsystem. Therefore, the concept of a cross section is not applicable and instead the differential invese inelastic mean free path (DIIMFP) is used to characterize the distribution W_b of energy losses T per unit pathlength, where the subscript "b" denotes losses that occur within the bulk of the solid.

Compared to the elastic scattering process described earlier, in the present case the energy losses arise from the deceleration of the incoming electron in the polarization field set up by the loosely bound solid-state electrons. This polarization field in turn is the solids response to the field of the incoming electron. The polarizability of the solid is described by the dielectric function $\epsilon(\omega, q)$, where $\hbar\omega = T$ is the characteristic excitation energy T absorbed by the solid and $\hbar q$ corresponds to the transfered momentum. The following equation relates $\epsilon(\omega, q)$ with the DIIMFP [34]:

$$W_\mathrm{b}(\omega, E) = \frac{1}{\pi a_0 E} \int_{q_-}^{q_+} \frac{\mathrm{d}q}{q} \, \mathrm{Im} \left\{ \frac{-1}{\epsilon(\omega, q)} \right\} \tag{II.22}$$

where E is the energy of the electron, a_0 is the first Bohr radius and $q_\pm$ are the upper and lower bounds of the momentum transfer, respectively, given by

$$q_\pm = \sqrt{\frac{2m}{\hbar^2}} \left(\sqrt{E} \pm \sqrt{E - T} \right)$$

.

The DIIMFP for aluminium for different electron energies is shown in figure II.12 on a semilogarithmic scale. One can see that the distribution is dominated by a sharp plasmon loss peak located at around $15\,\mathrm{eV}$, and for sufficiently high electron energies L-shell ionization occurs, giving rise to energy losses of approximately $70\,\mathrm{eV}$.

Aluminium is a metal with a particularly simple electronic structure and thus is its DIIMFP. Other metals may exhibit broader energy loss functions due to the more complicated band structures that allow inter- and intraband transitions.

In order to obtain a quantity equivalent to the EMFP in the sense that it corresponds to the MFP an electron travels before experiencing an inelastic collision event one must integrate over the DIIMFP, which gives the inverse of the inelastic mean free path (IMFP):

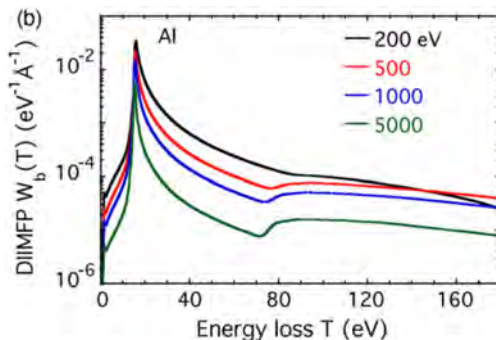$$\lambda(E)^{-1} = \int_0^\infty W_\mathrm{b}(T, E) \, \mathrm{d}T \tag{II.23}$$

Figure II.12.: Differential inverse inelastic mean free path (DIIMFP) for aluminium for different electron energies.

The expected value of the energy loss $\langle T(E) \rangle$ can be easily calculated through the first

algebraic moment of the normalized DIIMFP $w_{\mathrm{b}}(T, E) = W_{\mathrm{b}}(T, E)\lambda_{\mathrm{i}}$:

$$\langle T(E) \rangle = \int_0^\infty T w_{\mathrm{b}}(T, E) \, \mathrm{d}T \tag{II.24}$$

In figure II.12, showing the DIIMFP for aluminium, it can be observed that on the semilogarithmic scale the curves denoting different kinetic energies are virtually parallel for energies above $200 \, \mathrm{eV}$ and therefore in a first approximation the normalized DIIMFP $w_{\mathrm{b}}(T, E)$ can be seen as independent of the energy:

$$w_{\mathrm{b}}(T, E) \simeq w_{\mathrm{b}}(T) \tag{II.25}$$

Thus, the energy loss after n successive inelastic colisions is n times the expected energy loss:

$$\bar{E}_n = E_0 - n\langle T \rangle_n \tag{II.26}$$

with the initial energy E_0 of the electron. However, even though the expected energy loss can be seen as independent of the kinetic energy of the electron, the absolute values of the integral shown in equation II.23 and thus the IMFP depend on the kinetic energy of the electron. This means that electrons of different energies will experience approximately the same energy loss but after substantialy different traveled pathlengths. The energy loss per unit pathlength or the so-called stopping power can be written as:

$$\frac{\mathrm{d}T}{\mathrm{d}s}(E) = \frac{\langle T \rangle}{\lambda(E)} = \int W_{\mathrm{b}}(T)T \, \mathrm{d}T \tag{II.27}$$

The mean energy $\bar{E}$ as a function of the traveled pathlength is therefore

$$\bar{E}(s) = E_0 - \int_{s'=0}^s \frac{\mathrm{d}T}{\mathrm{d}s'} \, \mathrm{d}s' \tag{II.28}$$

Inverting this equation gives an expression for the mean pathlength traveled until a the initial energy decreases by T:

$$\bar{s} = \int_0^T \left(\frac{\mathrm{d}T}{\mathrm{d}s} \right)^{-1} \mathrm{d}T' = \int_0^T \lambda(E_0 - T') \frac{\mathrm{d}T'}{\langle T \rangle} \simeq (n+1)\Lambda_n \tag{II.29}$$

In this equation Λ_n is used as an approximation for the average mean free path after n collisions and is equal to

$$\Lambda_n = \frac{1}{n+1} \sum_{k=0}^n \lambda_k \tag{II.30}$$

where $\lambda_k = \lambda(\bar{E}_k)$ is the value of the IMFP after $k \leq n$ inelastic collisions accodring to equation II.23. In equation II.29 it is implicitly assumed that the energy loss is continuous and can be fully accounted for by the stopping power (see equation II.27), which is known as the continuous slowing-down approximation (CSDA). Differently put, in the CSDA the inherent fluctuations of the energy loss process are neglected and instead the energy loss

is accounted for by introducing a stopping power which depends merely on the traveled path length.

The average pathlength traveled by an electron before its energy falls below a certain cutoff energy E_c (e.g. $50\,\text{eV}$) can be calculated according to II.29 with different limits of integration and the resulting quantity is is the so-called linear range R:

$$R = \int_0^{E_0 - E_c} \left(\frac{\mathrm{d}T}{\mathrm{d}s} \right)^{-1} \mathrm{d}T \simeq (N+1)\Lambda_N \tag{II.31}$$

where N is the average number of inelastic collisions an electron undergoes within the linear range R:

$$N = \frac{E_0 - E_c}{\langle T \rangle} \tag{II.32}$$

In this context two energy regimes can be distinguished: The quasi-elastic (QE) regime where energy losses (or, equivalently, traveled path lengths or collision numbers) are small compared to the kinetic energy of the electron and thus the physical quantities governing the electron transport, such as the IMFP, the stopping power etc. are constant. In the true slowing-down (SD) regime this assumption does not hold and the energy dependence of the respective physical quantities have to be taken into account.

5.2. Landau-Goudsmit-Saunderson loss function

As described above, the CSDA fails to correctly account for the inherently occuring fluctuations of energy losses by establishing a fixed relationship between the energy loss and the traveled path length. According to the CSDA there would be no elastic peak in an electron spectrum since the signal electrons always experience a non-vanishing energy loss after traveling a finite pathlength. However, energy loss processes are stochastic processes and it is therefore necessary to describe these phenomena by means of stochastic methods.

The Landau-Goudsmit-Saunderson (LGS) loss function succeeds in describing these fluctuations arising from multiple elastic and inelastic scattering events in both energy and direction of motion as a function of the travelled pathlength within infinite media. The LGS loss function consists of two parts: The first, the Landau-part $G(s,T)$, covers the energy loss as a function of the pathlength, while the Goudsmit-Saunderson-part $Q^\infty(s,\mu)$ accounts for the distribution of pathlengths s traveling in an infinite medium, where μ is the polar direction $\mu = \cos\theta$. Together, both parts constitute the LGS loss function $G(s,T,\mu)$. In this section a brief overview over the derivation of the LGS loss function is given.

The probability $W_n(s)$ for n-fold scattering as function of the traveled pathlength can

be written for both aforementioned approximations [**?**]:

$$W_n^{\mathrm{QE}}(s) = \mathcal{P}_n(s) \equiv \frac{e^{-s/\lambda}}{n!} \left(\frac{s}{\lambda}\right)^n \tag{II.33}$$

$$W_n(s) = \mathcal{W}_n(s) \equiv \frac{\lambda_n}{\Lambda_n} \frac{e^{-s/\Lambda_n}}{n!} \left(\frac{s}{\Lambda_n}\right)^n \tag{II.34}$$

where $\mathcal{P}_n(s)$ and $\mathcal{W}_n$ stand for the scattering probabilities in the quasi-elastic and slowing-down regimes, respectively. Figure II.13 shows the probabilities for n-fold scattering of
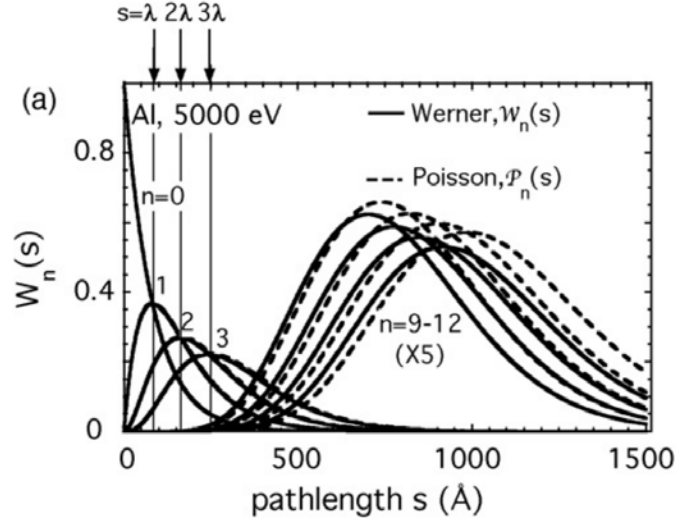

Figure II.13.: Probabilities for n-fold scattering as a function of the traveled pathlength s for 5 keV electrons in aluminium. Dashed curves correspond to the quasi-elastic regime given by equation II.33 while the solid corves correspond to the real slowing-down regime given by equation II.34.

5 keV electrons travelling through aluminium according to equations II.33 and II.34. The areas under the curves denoting n-fold scattering are equal to λ_n (or λ in the case of the QE approximation). Also, the maxima of collision order $n + 1$ intersect with lines of collision order n at multiples of the IMFP. One can see that the differences between the QE and the SD approximation become significant at collision orders of approximately $n = 10$. Below this value the probabilities for n-fold scattering are indistinguishable between the two cases. However, most importantly, the SD-approximation fully accounts for the fluctuations of the IMFP as the energy of the electron decreases with each consecutive collision.

In order to calculate the energy loss arising from n-fold scattering, in addition to knowing the collision statistics, it is necessary to factor in the distribution of the energy losses. Each collision, as described by equation II.34 is accompanied by an energy transfer and its magnitude is governed by the normalized differential mean free path $w_b(T)$ (see equation II.24). Therefore, the distribution Γ_1 of a delta-distributed energy profile after

the first collision can be written as:

$$\Gamma_n(T) = w_{\mathrm{b}}(T) \tag{II.35}$$

Thus, the distribution $\Gamma_n(T)$ of energy losses after n collisions is the n-fold self-convolution of the differential mean free path:

$$\Gamma_n(T) = \int_{\infty}^{\infty} \Gamma_{n-1}(T - T') w_{\mathrm{b}}(T') \, \mathrm{d}T' \tag{II.36}$$

The partial loss distribution Γ_n for $5\,\mathrm{keV}$-electrons in aluminium is shown in figure II.14, which is clearly dominated by the bulk plasmon losses giving rise to energy transfers of approximately $15\,\mathrm{eV}$ per inelastic collision.

For a given pathlength and collision number n the energy loss distribution can be easily calculated by taking the product of the probability for n-fold scattering $W_n(s)$ and the energy loss distribution $\Gamma_n(T)$. By summing over all possible collision numbers the Landau loss function in the form of a collision number expansion is obtained:

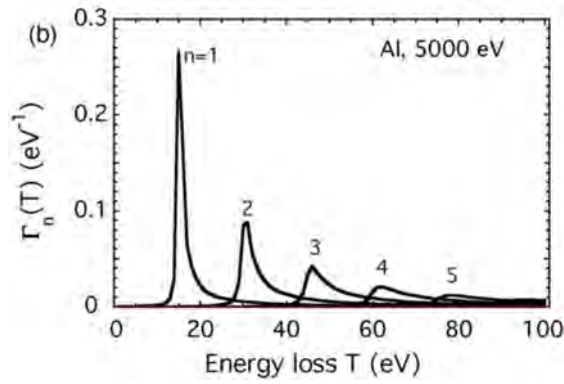$$G(s, T) = \sum_{n=0}^{\infty} W_n(s) \Gamma_n(T) \tag{II.37}$$

Figure II.14.: Partial energy losses Γ_n for $5\,\mathrm{keV}$-electrons in Aluminium

This equation constitutes the Landau-part of the LGS loss function. If elastic-scattering effects were not present, and an electron would therefore reach every point in space via a rectilinear path, this expression would constitute the basis for the caluclation of an XPS-spectrum. In contrast to the CSDA it incorporates the stochastic nature of the energy loss processes and explains the presence of elastic peaks. However, due to elastic scattering the pathlength an electron travels as it moves from some point A to some other point B in space is not always the same. Therefore, the pathlength distribution $Q(s, \mu)$ must be taken into account to correct for these fluctuations. In complete analogy to the previously derived Landau loss function the pathlength distribution of a infinite medium for a given direction of motion can be given by:

$$Q^{\infty}(s, \mu) = \sum_{n_{\mathrm{e}}=0}^{\infty} W_{n_{\mathrm{e}}}(s) \Gamma_{n_{\mathrm{e}}}(\mu) \tag{II.38}$$

In this context the subscript "e" denotes elastic scattering, $\Gamma_{n_{\mathrm{e}}}(\mu)$ the n-fold self-convolution of the elastic-scattering cross section on the unit sphere and $W_{n_{\mathrm{e}}}(s)$ the multiple scattering probability for elastic scattering.

Since elastic and inelastic scattering events are independent, equations II.37 and II.38 can be combined, forming the complete LGS loss function:

$$G(s, T, \mu) = \overbrace{\sum_{n=0}^{\infty} W_n(s) \Gamma_n(T)}^{\text{Landau Loss function}} \underbrace{\sum_{n_e=0}^{\infty} W_{n_e}(s) \Gamma_{n_e}(\mu)}_{\text{Goudsmit-Saunderson part}} \qquad \text{(II.39)}$$

Figure II.15 shows both contributions of the LGS, the Landau part on the left and the Goudsmit-Saunderson part on the right, for 500 eV electrons in the QE energy regime. The Landau part was calculated for aluminium and shows very clearly the energy losses due to plasmon losses which, in the case of aluminium and its simple DIIMFP, occur at multiples of the IMFP.

The Goudsmit-Saunderson part is based on calculations for gold and shows the dependence of the momentum relaxation process as a function of the traveled pathlength. With increasing pathlength the polar angle distribution becomes broad and featureless which implies that the particle has lost memory of its initial direction and thus satisfies the Markov-property. As shown in the figure, the characteristic length for this property is the TRMFP. It should be noted that equation II.37 can be applied universally while equation
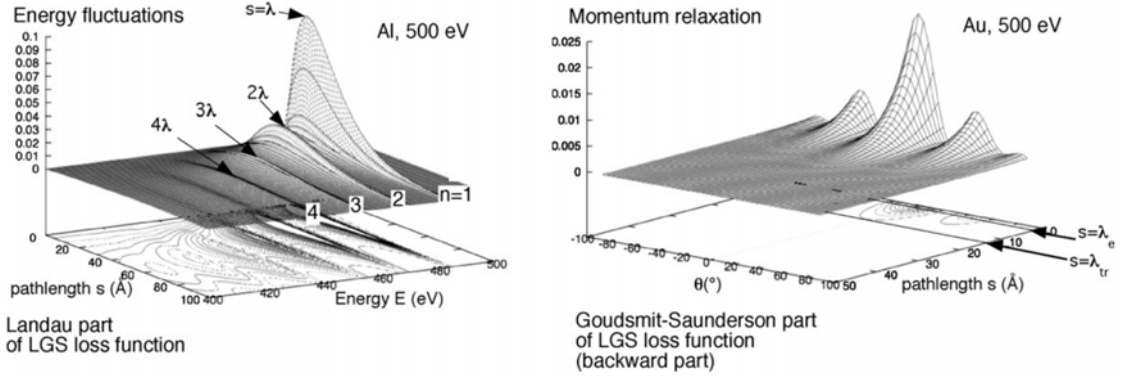

Figure II.15.: Forward- and backward parts of the LGS for 500 eV-electrons in aluminium and gold, respectively, in the quasi-elastic regime.

II.38, describing the pathlength distribution, is valid only for infinite media. However, the geometrical boundary conditions for a given transport problem have a critical impact on the pathlength distribution. Hence, for arbitrary geometrical boundaries one substitutes the backward part of the LGS loss function, $Q^{\infty}(s, \mu)$, by the pathlength distribution $Q(s, \mu)$, which gives the LGS loss function in a general form:

$$G(s, T, \mu) = \sum_{n=0}^{\infty} W_n(s) \Gamma_n(T) Q(s, \mu) \qquad \text{(II.40)}$$

Through this expression the electron transport problem is reduced to finding the path-

length distribution for the given geometry, which can be done most conveniently by means of a Monte Carlo simulation. If the pathlength distribution is know, then the observed spectrum can be obtained by integrating the LGS loss function over all possible pathlengths. For that purpose one can introduce the partial intensity $C_n(\mu)$, which is the number of electrons arriving at the detector after experiencing n inelastic collisions in the direction μ for a given problem.

$$C_n(\mu) = \int_0^\infty W_n(s) Q(s, \mu) \, ds \tag{II.41}$$

If the source energy distribution $f_0(E)$ is taken into account, the outgoing spectrum can be written as:

$$Y(E, \mu) = \sum_{n=0}^\infty C_n(\mu) \Gamma_n(T) \otimes f_0(E + T) \tag{II.42}$$

where the symbol $\otimes$ indicates a convolution over the energy.

The spectrum obtained through equation II.42 is usually affected by experimental factors, such as the transmission function of the spectrometer etc. However, by normalizing the partial intensities to the area of the no-loss peak these factors cancel out and one obtains the reduced partial intensities $\gamma_n(\mu)$:

$$\gamma_n(\mu) = \frac{C_n(\mu)}{C_{n=0}(\mu)} \tag{II.43}$$

Up to this point only bulk excitations were discussed, but the presence of a surface enables additional modes of excitation, namely surface excitations. Since surface and bulk excitations are uncorrelated, one can write for the partial intensities:

$$C_{n_\mathrm{b}, n_\mathrm{s}} = C_{n_\mathrm{b}} \times C_{n_\mathrm{s}} \tag{II.44}$$

where n_b and n_s are the bulk and surface collision numbers, respectively. The surface excitations obey Poisson statistics and can be written as:

$$C_{n_\mathrm{s}} = \frac{\langle n_\mathrm{s} \rangle^{n_\mathrm{s}}}{n_\mathrm{s}!} e^{-\langle n_\mathrm{s} \rangle} \tag{II.45}$$

With equations II.44 and II.45 equation II.42 can now be rewritten so that it incorporates surface excitation contributions:

$$Y(E, \mu) = \sum_{n_\mathrm{b}=0}^\infty \sum_{n_\mathrm{s}=0}^\infty C_{n_\mathrm{b}} C_{n_\mathrm{s}} \Gamma_{n_\mathrm{b}}(T') \otimes \Gamma_{n_\mathrm{s}}(T) \otimes f_0(E + T + T') \tag{II.46}$$

In conclusion, it can be stated that the LGS loss function constitutes the fundament for the Monte Carlo simulation engine employed in SESSA, and it allows to reduce the electron transport problem to finding the pathlength distribution of PEs for a given morphology.

5.3. Monte Carlo simulation engine in SESSA

The Monte Carlo method is a means to study electron transport problems by sampling large numbers of trajectories and analyzing parameters of this ensemble to obtain information on the physical quantities of interest. In this approach the stochastic nature of the electron-solid interaction within a given trajectory is accounted for by using random numbers to sample values for scattering angles and energy losses of individual collisions. In order to achieve statistical significance it is necessary to simulate large numbers of trajecotries, typically in the range of a few million trajectories. However, this number depends on the geometrical boundary conditions of the investigated problem and the applied approximations.

As shown in the preceeding section, the presented theory enables to calculate a full electron spectrum if the pathlength distribution $Q(s)$ is known, which can be most easily obtained through a Monte Carlo simulation. The basic procedure behind the simulation engine employed in SESSA is described hereafter.

For a single trajectory, the algorithm consists of three essential parts: First, the initial position of the electron is initialized according to the spatial distribution of sources and angular distribution of emission directions. Then, the particle is advanced by the pathlength s_e to the location of the next elastic collision. s_e is randomly sampled:

$$s_e = -\lambda_e \log R$$

where R is a random number between zero and unity and λ_e is the elastic mean free path of the current material. Also, a new scattering angle is randomly chosen from the distribution of angles for elastic scattering to determine the new direction of motion. Advancing the particle in this manner to points of subsequent elastic collision is repeated until an internal boundary is reached, the particle leaves the solid or until a predetermined number of collisions is reached, after which the trajectory is aborted since the contribution to the signal becomes negligible. If an internal boundary is encountered the particle position is reset to the intersection point and a new pathlength s_e is sampled using λ_e of the corresponding material. If the solid-vacuum boundary is crossed then it is checked if the direction of motion coincides with the acceptance angle of the detector. If yes, then the corresponding bin of the pathlength distribution $Q(s, \mu)$ is raised by unity. Otherwise the trajectory is dismissed and the next trajectory is sampled. It should be stressed that the simulation serves the sole purpose of determining the pathlength distribution $Q(s, \mu)$. The energy loss is factored in retrospectively by means of equations II.39 or II.41.

Despite the advanced computational capabilities of modern computers, it is sensible to employ measures to increase the efficiency of the simulation. In that context two major optimizations are implemented in SESSA: First, for simulation of XPS spectra one can increase not only the bin corresponding to some pathlength s_{traj} but also every bin with $s < s_{traj}$ since electron sources are present along the entire traveled pathlength and therefore every point of the trajectory contributes to the spectral feature. However, because of the anisotropy of the photoelectron emission one must weight each point accordingly.

The second contribution to a highly optimized Monte Carlo simulation stems from the fact that, in the described algorithm, only a fraction of the total number of trajectories is detected. Detection implies that the PE escapes the solid and is ejected into the detection cone of the analyzer. Most trajectories either do not leave the solid or are not ejected in a direction matching the detector acceptance angle and thus do not contribute to the signal. This problem can be addressed by means of the so-called reciprocity relationships for linear transfer, which allows to reverse the trajectory and overcome the described problems.

In contrast to conventional Monte Carlo codes where electrons are tracked on their trajectories from the source to the detector, the trajectory-reversal approach tracks electrons in the opposite direction, starting from the detector and following the trajectory back to the point of origin [35]. Thus, all electrons contribute to the signal resulting in significantly decreased simulation times, typically in the range from seconds to several minutes, depending on the number of peaks to be simulated and the desired precision in the results.

6. SESSA

SESSA is a standard reference database distributed by the National Institute of Standards and Technology containing all data needed for quantitative simulations of XPS and Auger-electron spectra [9, 10]. Data retrieval is based on a powerful expert system that queries the databases and provides the data to the user or the simulation engine for arbitrary sample morphologies and experimental settings. The simulation engine is a particularly crucial part of SESSA as it enables the user to conduct batch simulations of arbitrarily shaped nanostructures.

The extensive capabilities of SESSA Version 2.0 for simulating various nanomorphologies are based on the PENGEOM package, a general-purpose geometry package that allows one to define quasi-arbitrary geometries using quadric surfaces. PENGEOM comes as a stand-alone part of the PENELOPE code system which is widely used for simulation of electron and photon transport processes [36]. Based on the information provided by the user, a geometry file is created by SESSA and internally passed to PENGEOM which initializes the geometry, stores it in memory and provides various functions for tracking the electron trajectory. The geometry definition is based on a simple syntax with which surfaces such as planes, spheres, hyperboloids etc. can be defined and subsequently used to delimit phases of a material. Existing phases can be further used as building blocks for larger structures.

The recently released version V2.0 does not yet provide the option to load externally defined geometry files; however, this feature will be implemented in the upcoming version V2.1. The possibility to simulate externally defined geometries further expands SESSA's application possibilities as it, for example, enables the simulation of XPS intensities of lithographically manufactured structures using hard XPS. Currently the following morphologies are predefined and can be chosen: planar, roughness, islands, spheres and layered spheres. The planar and roughness morphologies are comprised of an arbitrary

number of stratified layers placed on a semi-infinite substrate. The composition and thickness of each layer can be easily changed by the user and SESSA always provides estimates for all needed material properties. For the roughness morphology, an additional parameter is defined to account for the increase in relative surface area (RSA) of a rough surface compared to a perfectly planar specimen. The increase in signal intensity due to an increased surface area is accounted for with the RSA parameter. The island and sphere morphologies enable one to simulate structures placed on a layered sample as in the case of a planar morphology.

For islands, the simulated structure consists of a trapezoid with variable dimensions in x, y and z directions together with variable inclinations of the side-walls. In the case of spheres, the dimensions of the sphere and its composition can be varied. The layered-spheres morphology allows one to simulate a spherical particle consisting of an inner core with an arbitrary number of overlayers. The dimensions of the sphere as well as the composition and thickness of each layer can be chosen by the user. All nanomorphologies are simulated as periodic arrays where the periods can be selected to represent isolated or dense assemblies of features.

As shown in our prior work [37] and by Frydman *et al.* [38], the surface of a dispersed powder of CS NP seen by a detector is equivalent to the surface of a single sphere and is independent of the viewing angle by the detector. Therefore, a simulation for a well-dispersed array of CS NPs yields the same ratio of photoelectron intensities from the core and the shell as from a bulk powder.

As described earlier, the Monte Carlo simulation engine works in the trajectory-reversal picture to ensure maximum computation and time efficiency of the simulation [35].

The graphical user interface of SESSA is shown in figure II.16, which is designed in a modular form.

Figure II.16.: SESSA's modular graphical user interface

In order to conduct a simulation a novice user simply needs to click each button, which will open dialog windows where all settings related to the respective part of the simulation can be edited. In the "Sample" window (shown in figure II.17, the user can choose the predefined geometries from a drop-down menu and after selecting the desired morphology a graphical visualization is shown below. For each layer, the thickness, the number of valence electrons, atoms per molecule as well as the atomic density and a band gap of the materials can be chosen. In the same manner the subsequent menus "Peaks", "Parameters", "Source", "Configuration", "Spectrometer" and "Simulation" allow to adjust all essential parameters for a simulation.
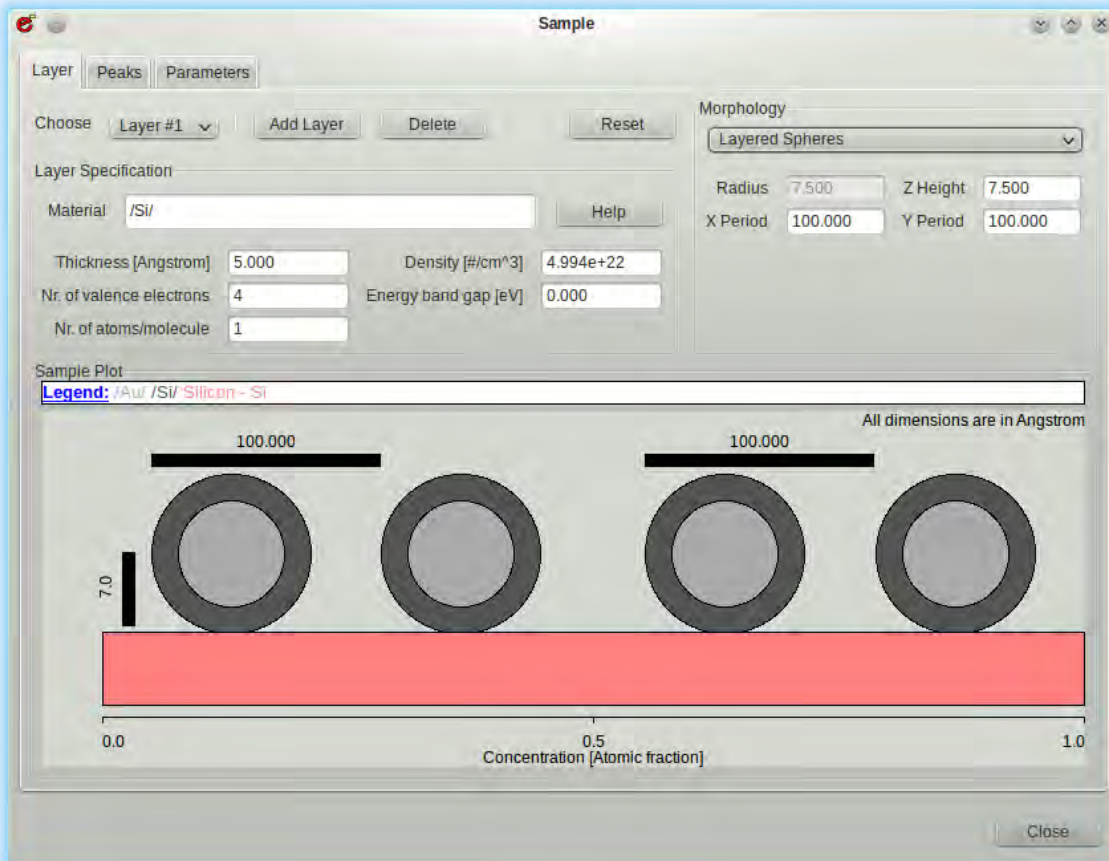
Figure II.17.: SESSA's sample window with a graphical visualization of the simulated morphology

For the more advanced user, a command-line interface (CLI) is available, which serves two purposes: First, every parameter that is adjusted is represented by a text-command which is displayed in the CLI, that is, if the user sets a particular morphology, the corresponding command will show up in the CLI-window. After conducting a simulation all the entered commands can be saved to a session-file which can be loaded at a later time to reproduce the same settings. Second, the CLI enables one to completely omit the graphical user interface by running SESSA from the command line with an additional parameter and supplying a ASCII-file containing the settings of a simulation. By doing so, it is possible to conduct large numbers of simulations, where for example a single parameters is changed (e.g., the thickness of a contamination layer) and the result of each simulation is saved to a predefined location, in order to be processed further with other software.

III.Results

1. Evaluating SESSA usings Shard's method

1.1. Shard's method

Shard [8] addressed the general problem of interpretation of XPS intensities of CS particles by establishing a simple and non-iterative procedure, the $T(\mathrm{NP})$ formula, that enables one to directly convert peak-intensity ratios to shell thicknesses in two-component systems. Emphasis was put on CS particles as they constitute a particularly important field of research due to their many applications [39–44].

The parameters in the $T(\mathrm{NP})$ formula are A, the ratio of the normalized XPS peak intensities from the shell and core materials, respectively, the radius R of the core, and the electron attenuation lengths L of the core and shell photoelectrons in each material. For normalization of the peak intensities I_i, calculated or experimentally determined intensities of the pure materials can be used and are written as I_i^∞. Following the notation in Shard's work, the subscript $i = 1, 2$ is used to identify photoelectrons arising from the shell and core materials, respectively, giving the normalized peak-intensity ratio A as:

$$A = \frac{I_1 I_2^\infty}{I_2 I_1^\infty} \tag{III.1}$$

Shard's approach for obtaining an expression for the shell thickness of a CS NP was to make approximations for overlayer thicknesses of different limiting cases, such as planar samples, infinitesimally small particles (see eq. (III.4)), or macroscopic particles (see eq. (III.3)). The formula for calculation of nanoscopic CS particles was obtained by combining these limiting cases. The fit parameters α and β were determined by validating the results with numerical calculations, so that the validity of the resulting formula is ensured within the limits of the model and the relevant core radii and shell thicknesses. The resulting $T(\mathrm{NP})$ formula is given by:

$$T_{Shard}(A) = \frac{\dfrac{T_{R\to\infty}}{R + \alpha} + \beta\, T_0}{1 + \beta} \tag{III.2}$$

$$T_{R\to\infty} = \frac{0.74\, A^{3.6} \ln(A)\, B^{-0.95} + 2AB^{-0.42}}{A^{2.2} + 1.9} \tag{III.3}$$

$$T_0 = R\left[(ABC + 1)^{1/3} - 1\right] \tag{III.4}$$

The values of α, β, B and C are defined by equations (III.5) to (III.8) below, and depend on the attenuation lengths of the particular material system. Here $L_{i,j}$ is the attenuation length of photoelectrons originating from material i and currently moving through material j. All quantities with the dimensions of length are given in units of

$L_{1,a}$, the attenuation length of the overshell material photoelectrons within the overlayer.

$$\alpha = \frac{1.8}{A^{0.1}B^{0.5}C^{0.4}} \tag{III.5}$$

$$\beta = \frac{0.13\,\alpha^{2.5}}{R^{1.5}} \tag{III.6}$$

$$B = \frac{L_{1,a}}{L_{2,a}} \tag{III.7}$$

$$C = \frac{L_{2,a}}{L_{2,b}} \tag{III.8}$$

Equation (III.2) enables one to calculate the shell thickness of a CS NP given the (experimental) normalized intensity ratio, the attenuations lengths $L_{i,j}$ of the core and shell materials, as well as the core radius. Both the attenuation lengths and the pure elemental intensities I_i^∞ needed to calculate the normalized intensity ratio A are easily retrieved using SESSA by running simulations or querying the expert system. Equation (III.2) applies to radii of NPs ranging from approximately 1 nm to 1 μm and provides shell thicknesses with a typical standard uncertainty of 4 %. This uncertainty is considerably smaller than the typical uncertainty of the attenuation lengths $L_{i,j}$, that are based on inelastic mean free paths with estimated uncertainties of about 10 % [45].

1.2. Procedure

In order to evaluate the $T(\mathrm{NP})$ formula, the following approach was adopted: For a given shell thickness, T_{SESSA}, core radius R, and material composition of the CS system, a simulation was conducted using SESSA, yielding a simulated value for the normalized intensity ratio, A_{SESSA}. Using this value for A_{SESSA} in eq. (III.2), together with the core radius R and the constants B and C, the calculated shell thickness T_{NP} is obtained. In the ideal case T_{SESSA} and T_{NP} are equal, and a plot of T_{SESSA} as a function of T_{NP} yields a straight line with unity slope through the origin.

The $T(\mathrm{NP})$ formula was used to investigate the two previously described model systems consisting of a weakly scattering beryllium shell on a gold core (system 1) and a palladium shell on an aluminum oxide core (system 2), respectively. The evaluation was conducted for four different core radii as displayed in figure III.1. For each case, 50 simulations were conducted with varying shell thicknesses in the range from $0.1\,L_{1,a}$ to $5\,L_{1,a}$ in steps of $0.1\,L_{1,a}$.

The values of $L_{1,a}$ for systems 1 and 2 were 3.15 nm and 1.20 nm, respectively. $L_{1,a}$ also determines the size of the simulated CS NPs as T and R are given in units of $L_{1,a}$. Figure III.1 displays the four different CS particle systems used in the simulations. The figure is given to scale to emphasize the wide range of radii employed for the evaluation. The corresponding sizes for each material composition can be found in table III.1. It is important to note that with a shell thickness of $5\,L_{1,\mathrm{a}}$ the XPS intensity from the core will almost certainly be too weak to measure in practice. For this reason the $T(\mathrm{NP})$ formula was only validated using the SLA up to $\approx 3\,L_{1,\mathrm{a}}$ in the original work [8] but,

Table III.1.: Minimum and maximum diameters of the Be/Au and Pd/Al$_2$O$_3$ CS NPs for each core radius, according to figure III.1. The minimum and maximum values depend on the shell thickness, which ranged from 0.1 $L_{1,a}$ to 5 $L_{1,a}$

Core radius R	Be/Au		Pd/Al$_2$O$_3$	
	min. diameter [nm]	*max. diameter* [nm]	*min. diameter* [nm]	*max. diameter* [nm]
0.5 $L_{1,a}$	3.79	34.71	1.44	12.23
1 $L_{1,a}$	6.94	37.86	2.65	14.43
8 $L_{1,a}$	51.11	82.03	19.49	31.27
32 $L_{1,a}$	202.55	233.47	77.22	89.01

because the formulation is accurate in at least some of the extremes of core radii and shell thicknesses, we may expect it to be valid over a wider range.

1.3. Results

Figure III.2 displays the results of the evaluation in form of a plot displaying T_{NP} against T_{SESSA} for the Be/Au and Pd/Al$_2$O$_3$ CS NPs for cases **I**, **II**, **III** and **IV** of figure III.1 and the range of shell thicknesses described above. The red dotted lines consist of 50 discrete points each corresponding to an independent simulation. Two sets of simulations were performed for each set of materials, core radii, and shell thicknesses, one accounting for elastic-scattering effects (b and d) and one with the SLA (a and c) where all electron trajectories follow rectilinear paths. Values of T_{SESSA} and T_{NP} were normalized to the appropriate value of $L_{1,a}$.

As seen on the left side of figure III.2, few significant deviations occured between T_{NP} and T_{SESSA} for the Be/Au system, both when elastic scattering was accounted for and when the SLA was employed since the shell is a weakly scattering material. That is, most trajectories are close to rectilinear.

It should be stressed that the $T(\mathrm{NP})$ formula is based on the SLA and does not account for elastic scattering. For the Be/Au model system, there is generally good correlation between T_{NP} and T_{SESSA}. Some small deviations, however, were found at relatively large shell thicknesses ($T/L_{1,a} \geq 3$) and a core radius of $R = 0.5\,L_{1,a}$, as shown in panel **IVa** in figure III.2. The deviations, however, appear at shell thicknesses which are beyond the limits of the $T(\mathrm{NP})$ formula, which was established for shell thicknesses of approximately $T/L_{1,a} \leq 3$ [8].

For Pd/Al$_2$O$_3$ NPs the shell material has a high atomic number and stronger elastic-scattering effects are expected [46]. Elastic scattering leads to deflections of photoelectrons emitted from the core material and therefore a lower core signal, thus resulting in an overestimate of the shell thickness using the $T(\mathrm{NP})$ formula. A comparison between results of simulations conducted with and without the SLA in figure III.2 shows this effect very convincingly.
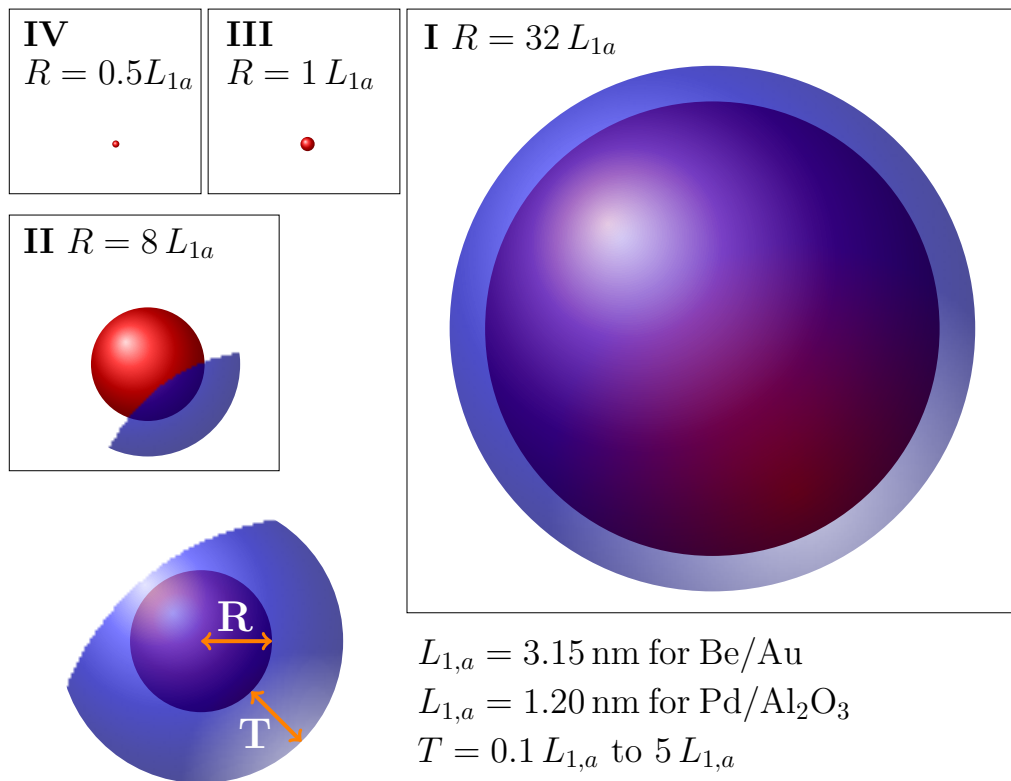
Figure III.1.: To scale representation of the four CS systems used for the evaluation of the $T(\text{NP})$ formula. The definition of the core radius R and the shell thickness T are displayed in the bottom left corner. The actual size depends on the chosen shell material as all dimensions are given in units of $L_{1,a}$, the attenuation length of shell photoelectrons within the shell. For both model systems, the values of $L_{1,a}$ are listed at the bottom. In all four cases **I–IV**, the shell thickness T is depicted with a constant thickness of $5\,L_{1,a}$ while the simulations were conducted for values ranging from $0.1\,L_{1,a}$ to $5\,L_{1,a}$. The core radii for cases **I** to **IV** are respectively: **I**: $R = 32\,L_{1,a}$, **II**: $R = 8\,L_{1,a}$, **III**: $R = L_{1,a}$, **IV**: $R = 0.5\,L_{1,a}$
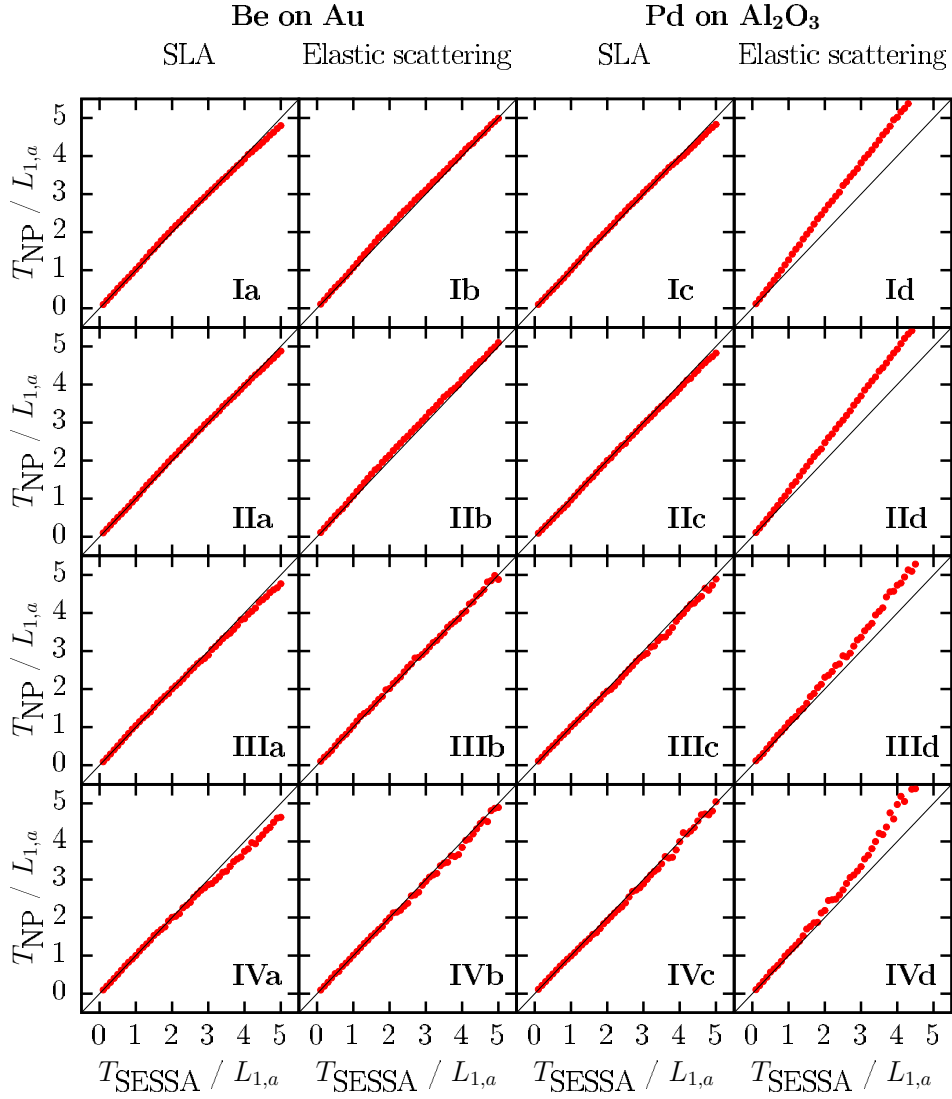
Figure III.2.: T_{NP} plotted against T_{SESSA} for the Be/Au and the Pd/Al$_2$O$_3$ NP systems of figure III.1. T_{NP} was calculated according to eq. (III.2) using the normalized intensity ratio A_{SESSA} obtained from a simulation conducted with the shell thickness T_{SESSA}. Every red dot corresponds to a simulation at a different shell thickness, ranging from $0.1\,L_{1,a}$ to $5\,L_{1,a}$. For each material system the plots on the left side were conducted with the SLA, whereas the plots on the right side depict simulations with elastic scattering. The roman numerals correspond to the numerals in figure III.1.

The simulations denoted by **Ic** to **IVc** were carried out using the SLA and in this case there are no significant differences between T_{NP} and T_{SESSA}. The deviations from this ideal behavior due to elastic-scattering effects manifest themselves very clearly in the **Id** to **IVd** panels.

This effect can be explained by comparing the relative contributions of core and shell photoelectrons of two CS NPs with different radii but constant shell thickness, as shown in figure III.1-**I** and III.1-**IV**. For a very small core radius, the whole core contributes to the signal in equal measure. Also, the relative shell intensity is then much larger as the shell comprises most of the CS particle volume. However, given a large core radius with the same shell thickness, most of the core intensity originates from the region just beneath the shell. As a first approximation, the relative volume ratio of the core and shell regions contributing to the signal and the normalized intensity ratio A are both closer to unity than in the former case. The attenuation of the core signal due to elastic scattering has a larger impact on larger particles as the signal contribution from the core increases. This behavior is also reflected in eq. (III.3), which has a logarithmic contribution in A. The value of A, giving the shell-to-core ratio of photoelectron intensities, is large for small particles where the shell is dominant. Since the shell-to-core ratio A has a logarithmic contribution to the $T(\mathrm{NP})$ formula, as seen in equations (III.2) and (III.3), the error in the calculated shell thickness will be large for small values of A, while for large values of A the error will be negligible. Thus, when A is close to unity, small changes in A have a large effect on its logarithm, leading to deviations at smaller shell thicknesses.

The $\mathrm{Pd}/\mathrm{Al}_2\mathrm{O}_3$ material system was also studied with regard to the influence of a 0.15 nm carbonaceous contamination layer on the normalized intensity ratio and the predicted shell thickness. It was found that the results obtained with and without the thin contamination layer were indistinguishable for all cases, meaning that the presence of a thin carbonaceous contamination layer does not affect the result obtained with the $T(\mathrm{NP})$ formula, given that the contamination is the only carbonaceous compound of the CS system. Thicker contamination layers, which approach the electron attenuation length in thickness, will affect the accuracy of the $T(\mathrm{NP})$ calculation. Such situations can be classed under the general case of core-shell-shell systems. These may be easily modelled using SESSA but significant modifications to the $T(\mathrm{NP})$ approach are required to deal with such systems. As shown later in fig III.9, such a contamination layer has a large influence on the normalized intensity ratio if carbon is present within the core or shell.

In summary the $T(\mathrm{NP})$ formula performs very well on systems where applying the SLA is justified, such as gold NPs functionalized with alkanethiols. However, the method has relatively large uncertainties (up to 25 % in panels **Id** to **IVd** of figure III.2) in the shell thicknesses of material systems comprised of a strongly scattering shell since the $T(\mathrm{NP})$ formula is based upon the assumption of rectilinear electron trajectories.

2. Simulation Core-Shell Nanoparticle XPS intensities of different structures

In this chapter the results obtained with SESSA 2.0 for differently aligned CS particles are presented. The simulations were carried out for different structures of CS particles which can be grouped into periodic and dispersed arrangements and which can be seen in figure III.3.

The periodic arrangements consisted of regular structures which exhibited a strict spatial periodicity, such as checkerboard-like arrangements of CS particles with one, two, or three layers which were stacked in form of a primitive cubic cell.

On the other hand, the dispersed structures consisted of sub-monolayers of CS particles and powder-like structures. In the former case, which constitutes the counterpart to the regularly aligned monolayer of CS particles, the correlations along the lateral coordinates was relaxed. Several simulations with varying surface coverage werer carried out, where the surface coverage denotes the fraction of CS particles located in a unit cell, relative to the number of regularly aligned CS particles. In the case of powder-like structures a number of randomly sampled morphologies was simulated because each morphology has distinct features which lead to features in the polar angle distribution. Therefore, by simulating different disperse morphologies one obtains a representative average.
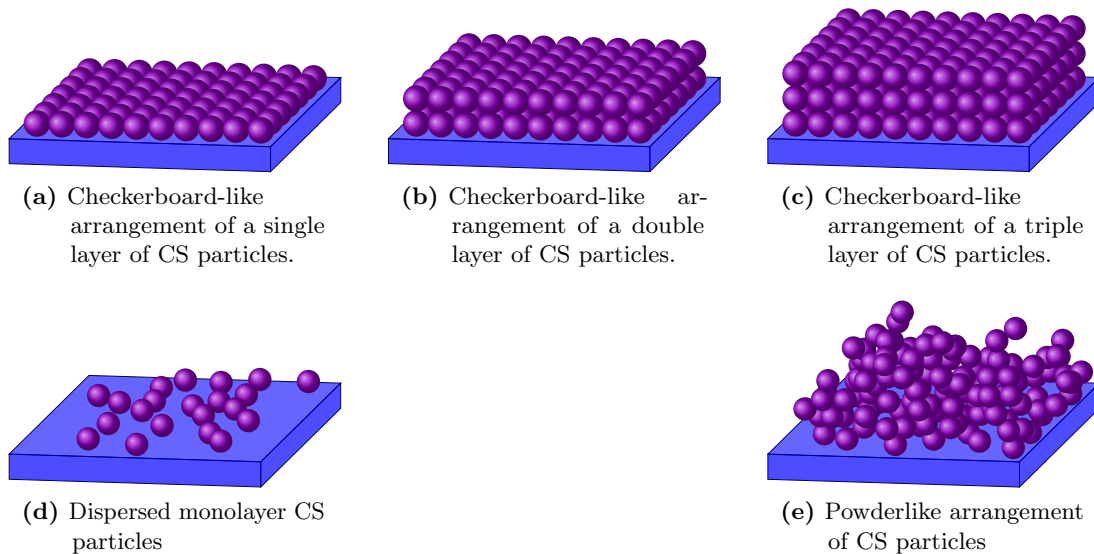
(a) Checkerboard-like arrangement of a single layer of CS particles.

(b) Checkerboard-like arrangement of a double layer of CS particles.

(c) Checkerboard-like arrangement of a triple layer of CS particles.

(d) Dispersed monolayer CS particles

(e) Powderlike arrangement of CS particles

Figure III.3.: Illustrations of different morphologies comprised of different arrangements of CS particles used for the simulations with SESSA.

A illustration of the internal structure and the nomenclature used for denoting the shell thicknesses and radii of CS particles can be found in III.1. If not stated otherwise, the dimensions of the CS particles used within the simulations were $T = 1.5$ nm and $R = 2$ nm. Also, the SLA was employed for all simulations, as it qualitatively gives the same results

as simulations with elastic scattering, however, the statistics of the simulation results are better in the former case.
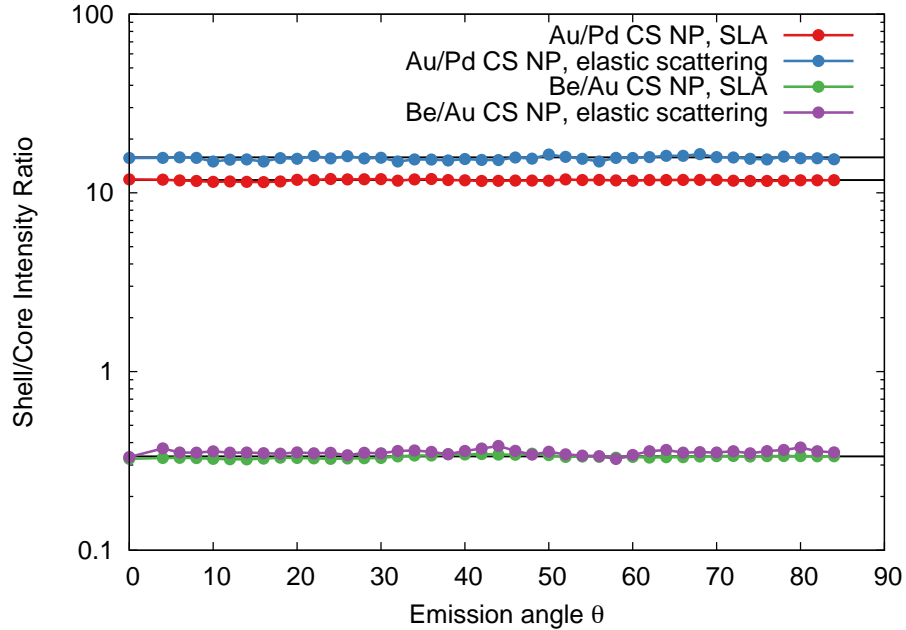
2.1. Impact of Elastic scattering

Figure III.4.: Polar angular distribution of the $Au4f_{7/2}/Pd3d_{5/2}$- and $Be1s/Au4f_{7/2}$- intensity ratios of single Pd/Au and Be/Au CS NPs with standard dimensions.

Figure III.4 displays the polar angular distribution of the $Au4f_{7/2}/Pd3d_{5/2}$- and the $Be1s/Au4f_{7/2}$-intensity ratio (i.e., the shell-to-core ratio) of single core-shell NPs with and without the SLA. In this context, it should be stressed that simulating the XPS spectrum of a single sphere is experimentally impossible, however, as mentioned in the introduction, a single sphere is a viable model for simulating the photoelectron peak intensities, since the photoelectron peak intensity ratio obtained from this model system is identical to intensity ratio obtained from a powder. However, as will be shown later, the intelastic background of a photoelectron spectrum originating from a single sphere is intrinsically different from a bulk powder of CS particles.

Since a single sphere looks identical irrespective of the direction of observation, the resulting angular distribution of the photoelectron peak intensity ratios give straight lines for both the straight line approximation and elastic scattering, but depending on the material system significant deviations in the photoelectron peak intensity ratio can occur when the SLA is employed, i.e. one neglects elastic scattering. In figure III.4 one can see that the photoelectron peak intensity ratio obtained from a Be/Au CS NP is nearly identical for both cases. This can be explained by the fact that Beryllium is a weak scatterer and thus the signal originating from the core material is not deflected

out of the detection cone as it propagates through the shell material. For the Au/Pd material system, which consists of a strongly scattering gold shell, the signal originating from the palladium core is significantly attenuated in the case where elastic scattering is accounted for, and therefore the shell-to-core ratio is shifted in favor of the shell material compared to the SLA.

The SLA is a commonly employed simplification, which often greatly simplifies modelling, however, one should be aware of the introduced error. For instance, if the Au/Pd peak intensity ratios obtained for the SLA- and elastic scattering-case (ELS) are used in Shard's formula, the resulting shell thicknesses T are $16.9\,\text{Å}$ and $15.0\,\text{Å}$, respectively. Thus, the error resulting from neglecting elastic scattering, in this special case, amounts to 12%, or approximately $2\,\text{Å}$.

With SESSA 2.0 different material systems can be easily investigated in order to estimate the error arising from the SLA and possibly to correct for that error.

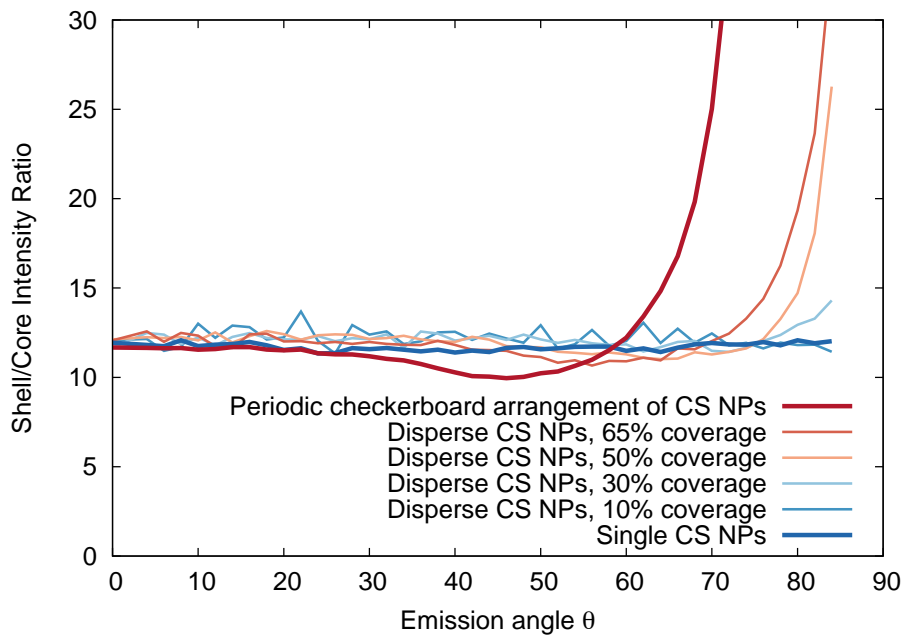## 2.2. Relationship between regular arrangements of CS NPs and dispersely arranged layers of CS NPs

Figure III.5.: Polar angle distribution of the $Au4f_{7/2}/Pd3d_{5/2}$-intensity ratios of CS NPs, ranging from a single CS NP (dark blue line) to a regular, periodic array of CS NPs (dark red line) with dispersely arranged arrangements with varying coverages (pale red to pale blue)

Figure III.5 illustrates the relationship between a regular checkerboard-like arrangement of CS NPs (dark red line) and a dispersely aligned arrangement of CS NPs with different suface coverages (pale red to pale blue lines). Also, the angular distribution of a single

CS NP is shown for comparison. The study of this relationship is important as dispersely aligned arrays of CS NPs constitute a realstic representation of real sub-monolayer samples of CS NPs.

For a surface coverage of 10% (i.e., 10 CS NPs occupying a unit cell that could accomodate 100 CS NPs) the angular distribution matches that of a single sphere. With increasing surface coverage, however, features in the angular distribution emerge and for high surface coverages the angular distribution begins to conicide with that of a periodic arrangement of CS NPs (see pale red lines in figure III.5).

The features of the periodic arrangement of CS NPs, i.e. the minimum at approximately 45% and the increase in shell intensity at emission angles beyond 60% can be explained as follows. At an emission angle of 0° the signal from both the shell and core materials is identical to the signal from a single CS NP. However, with increasing emission angle θ the shells of adjacent CS NPs start to shield each other, leading to a attenuated signal intensity originating from the shielded parts of the CS NP, while the core signal remains unattenauted due to the small emission angle. Only at larger angles the cores of adjacent CS NPs get shielded by neighboring NPs, and by virtue of this shielding-effect the minimum in shell/core-intensity at approximately 45° arises. The location of the minimum depends on the dimensions of the CS particles and the ratio between the core and shell thicknesses.

As shown in figure II.6, with increasing emission angle the emission depth decreases. Thus, the increase in shell/core-ratio can be attributed to the decreasing emission depth, which implies that a photoelectron emitted from the uppermost part of the core would have to pass through numerous CS particles in order to escape the material and get detected. Therefore, with increasing emission angle the shell intensity increases ad infinitum.

In the case of dispersely aligned CS NPs an increased surface coverage leads to higher ordering of the CS particles and as consequently to a qualitatively identical trend.

2.3. periodic structures (1lay, 2lay,3lay, FCC) - powder (var R, const R)

This section illustrates the relationship between regularly aligned multi-layer structures and dispersely aligned structures resembling powders comprised of CS NPs, in contrast to the previously discussed case of a sub-monolayer arrangement of dispersely arranged CS NPs. Also, the impact of a varying core- and shell thickness on the shell/core intensity was studied, since the synthesis of CS NPs always leads to a distribution of the dimensions of core- and shell-thicknesses.

Figure III.6 displays the polar angle distribution of a various multilayer arrangements of CS NPs (stacked as primitive cubic cells), a face-cubic-centered structure (FCC) and the distribution of a single sphere for comparison. The distinct features in the core/shell ratio of the different structures arise due to the correlation of the CS NPs along the spatial coordinates. The increase in shell/core ratio is again due to the low emission depth of signal electrons at large emission angles.
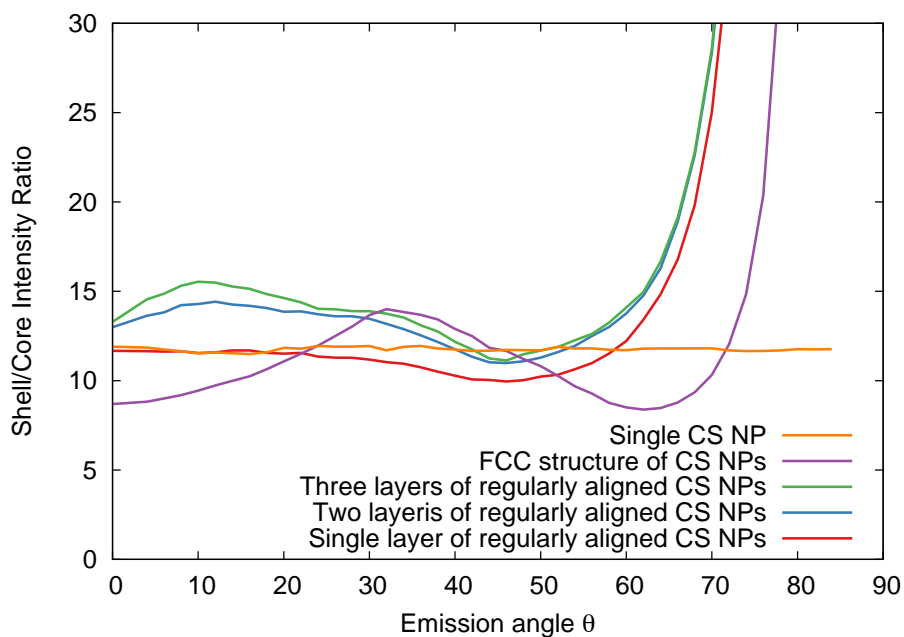
Figure III.6.: Polar angle distribution of various multilayer arrangements of CS NPs and a single CS NP for comparison.
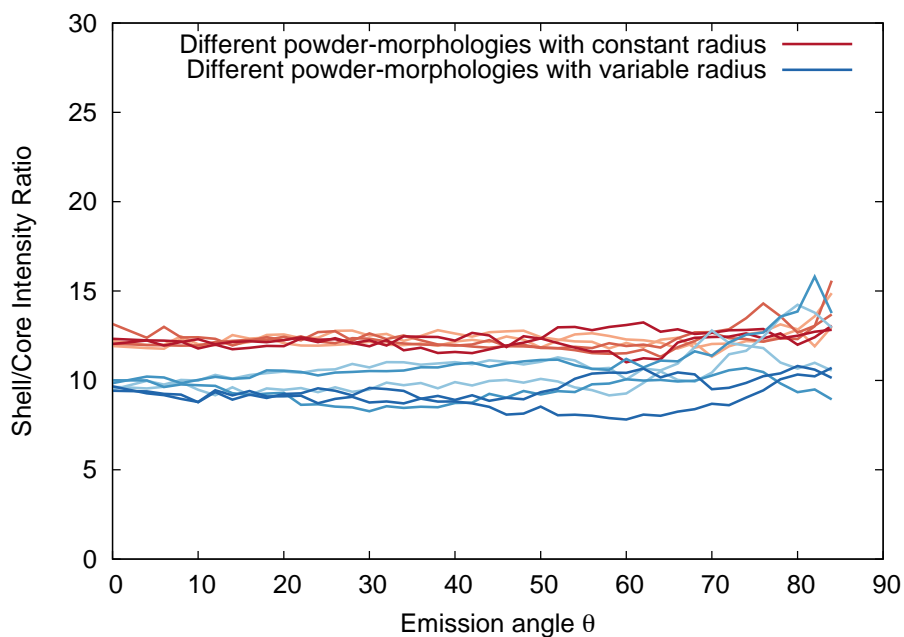

Figure III.7.: Polar angle distribution of different powder morphologies with constant (red lines) and variable radius (blue lines).

Figure III.7 shows the shell/core ratio of randomly aligned CS NPs, i.e. structures that resemble powders. In order to simulate such random, powder-like structures, a program was written which created geometry files representing such structures by randomly placing a predefined number of CS NPs within a large unit cell. A detailed explanation of the algorithm is given in appendix **??**.

In red, the angular distribution of a powder of CS NPs with standard dimensions of $R = 2$ nm and $T = 1.5$ nm is shown for an array of different morphologies. The shell/core intensity ratio is identical with the shell/core ratio obtained from a single sphere, showing that the photoelectron peak intensity of a single sphere (compare with figure III.6) is identical to that of a bulk powder. It should also be noted that the excursions from the expected, featureless distribution are not caused by the statistics of the Monte Carlo simulation, and can be attributed to the specific arrangement of the CS NPs within the morphology. The average over all red lines in figure III.7 gives a perfectly straight line, as in the case of a single sphere.

The blue lines in figure III.7 represent the shell/core ratio of powder samples with non-uniform dimensions. That is, the radii R and shell thicknesses T followed student-t distributions with means equal to the standard dimensions of $R = 20$ nm and $T = 15$ nm, and standard deviations equal to $\sigma_R = 10$ nm and $\sigma_T = 7.5$ nm, respectively. Such non-uniform size distributions of the CS NPs are a more realistic representation of a real powder-sample, since the synthesis of such particles always yields particles with non-uniform size distributions.

As shown in figure III.7, the impact of the non-uniformity of the particle dimensions has a considerable effect on the shell/core ratio, which is decreased by approximately 20%. However, the shift can be attributed to a increased core-signal, rather than a decreased shell-signal. Thus, the signal contribution from CS NPs with a thinner shell and consequently a less attenuated core signal give rise to a higher core signal. This result shows the importance of a Monte Carlo simulation for the simulation of agglomerates of CS NPs, which are always subject to non-uniform size distributions, which can have a significant effect on the intensity ratios of the investigated material systems.

3. Surface-sensitivity of XPS

SESSA 2.0 was used to study the relation between signal intensity and the surface to volume (S/V) ratio. For this purpose, a number of simulations was conducted with a defined volume of gold NPs. The first simulation was conducted with a single NP. The second simulation consisted of an array of 2×2 spheres with an overall volume equivalent to the volume of the first NP. In all further simulations the number of NPs was increased quadratically, while the total volume remained constant and by accordingly adapting the individual NP radius.

Figure III.8 shows the results obtained for the $Au4f_{7/2}$ peak intensity as a function of the NP radius. The S/V ratio of the NP is given by the solid black line which is proportional to $1/r$. Since XPS is a highly surface-sensitive technique, it is expected that the $Au4f_{7/2}$-intensity would increase proportionally with the S/V ratio. As shown in
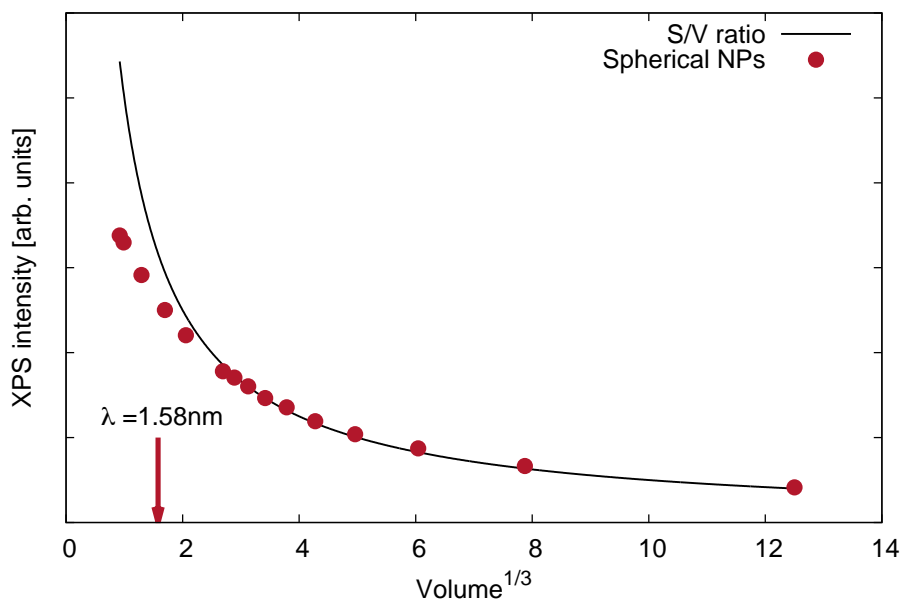
Figure III.8.: Au$4f_{7/2}$ peak intensity of spherical gold NPs as a function of the NP radius. Each red datapoint represents a simulation of gold NPs with decreasing radius but increasing number of NPs, so that the total volume of gold was constant throughout all simulations. The solid curve represents the surface to volume ratio, which is proportional to $1/r$. The vertical arrow indicates the IMFP of the Au$4f_{7/2}$ photoelectrons.

figure III.8 this relationship is valid for NP radii larger than the IMFP of the investigated peak. As the radius of the NP decreases to values close to the IMFP the intensities lie below the expected S/V ratio, which implies that XPS is no longer surface-sensitive but tends to be more volume-sensitive. This can be attributed to the fact that for such small NPs the volume of the sample is smaller than the escape volume of the photoelectrons.

4. Applying SESSA to experimental data

Self-assembled monolayers (SAMs) of alkanethiols on flat gold surfaces are a widely employed model system in nanotechnology due to their well-defined structure and surface properties. Numerous studies deal with the synthesis, characterization, thermodynamics, and reactivity of alkanethiols on flat gold surfaces but there are still many open questions regarding basic properties of SAMs on highly curved surfaces [40, 47–52].

Techane *et al.* [15] conducted a quantitative analysis of the SAM-layer thickness of 16-mercaptohexadecanoic acid ($C_{16}COOH$) on flat gold and on 14 nm diameter gold nanospheres using XPS for experimental measurements and SESSA Version 1.3 for simulations of the two systems. Since SESSA 1.3 did not provide means to simulate spherical particles directly, Techane *et al.* modeled a CS particle using nine concentric cylinders connected by flat, angled surfaces. These top surfaces, consisting of $C_{16}COOH$ overlayers attached to a semi-infinite gold substrate were simulated using SESSA 1.3. In order to get the correct peak intensities of the SAM on a gold NP, geometric weighting factors were applied to each simulated surface to account for the different areas.

With SESSA Version 2.0, simulation of CS NPs with an arbitrary number of shells becomes a matter of defining the compositions, thicknesses, and atomic densities of each layer with the help of a user-friendly graphical user interface. The simplicity of this approach enables users without detailed expertise in modeling to investigate systems of different nanomorphologies on a routine basis. In the present work, SESSA 2.0 was employed to model the data of Techane *et al.*

4.1. Simulation of SAMs with SESSA 2.0

Unlike a dense material, the atomic density of SAMs attached to highly curved surfaces decreases with the radius because of the spreading of the aliphatic chains. It should be noted that, on an atomic scale, gold NPs consist of (111) and (100) terraces and are therefore not perfectly spherical [53, 54]; however, in the course of this work the 14 nm gold NPs were assumed to perfectly spherical to facilitate the process of simulation with SESSA.

In Techane's model, the atomic density was assumed to be constant throughout the whole thickness of each concentric cylinder, since accounting for the changing density was not easily possible using their approach [15]. A decreased SAM density with radius of the gold NP could result in the enhanced mobility of the chains leading to defects and kinks in the structure of the SAM and a reduced thickness compared to the corresponding SAM on a planar substrate.

The goal of the work by Techane *et al.* was to obtain the best possible agreement between the experimentally derived and simulated normalized intensities by varying the thickness of the CH$_2$ groups and the relative surface area (RSA) parameter. This parameter accounts for the increase in surface area due to curvature or roughness of a otherwise planar surface and it was employed by Techane *et al.* as a second parameter to optimize results from their simulations.

In the work of Techane *et al.*satisfactory agreement between the simulated and experimental data required introduction of a CH$_2$-contamination layer. The signal contribution originating from this ubiquitous contamination layer significantly adds to the carbon signal from the deeper buried CH$_2$ shells and was required for good agreement. The impact of the contamination layer on the carbon intensity was studied using SESSA by simply adding or removing an additional hydrocarbon layer on top of the SAM.

We assumed that the gold NPs were perfectly spherical and had a diameter of 14 nm. This choice is based on transmission electron microscopy measurements that gave a size distribution of 14 ± 1.5 nm and a circularity (ratio of the major axis to the minor axis of the particles) of 1.09 ± 0.06 [15]. The surface density of the C$_{16}$COOH chains was $0.214\,\mathrm{nm^2}$/chain [15], which amounts to approximately 2877 chains attached to the surface of a single 14 nm NP. The atomic density within each layer was calculated in a way that, multiplying it by the volume of the shell, gives the total number of atoms occupying the shell, e.g., 2877 sulfur atoms in the innermost shell or 3×2877 atoms in each CH$_2$ shell. This method ensures that the total number of atoms equals the number of chains times the number of atoms per chain [15, supporting information]. The C$_{16}$COOH chains were assumed to be immobile and perfectly aligned, so that the only degree of freedom is the tilting angle relative to the normal which could affect the effective thickness of the CH$_2$ groups. Since the total number of atoms attached to a NP is constant, the tilt of the SAM can be imitated by reducing the thickness of the CH$_2$ shells and accordingly increasing the atomic density within the shells.

4.2. Results

Employing the same approach as Techane *et al.* [15], a number of simulations with different CH$_2$ thicknesses was conducted to find the thickness that provided the best agreement with experimental XPS data. Figure III.9 displays the normalized photoelectron intensities of each element from the SESSA simulation for CH$_2$ shell thicknesses ranging from 0.08 nm to 0.11 nm/CH$_2$ group together with the experimental data. We also show results for one case where the simulation was conducted without the hydrocarbon contamination layer in order to study the impact of this layer. There is generally good agreement between the experimental intensities and the simulated intensities when an additional contamination layer was included. The leftmost bar shows the simulated intensities when the hydrocarbon contamination layer was omitted. This omission had a considerable impact on the gold, carbon and oxygen intensities, as they are significantly over- or under-estimated compared to the experiment. Considering the minimal effort to set up and run the simulations, this result shows the capability of SESSA 2.0 in facilitating the simulation of systems composed of NPs. The experimentally determined normalized
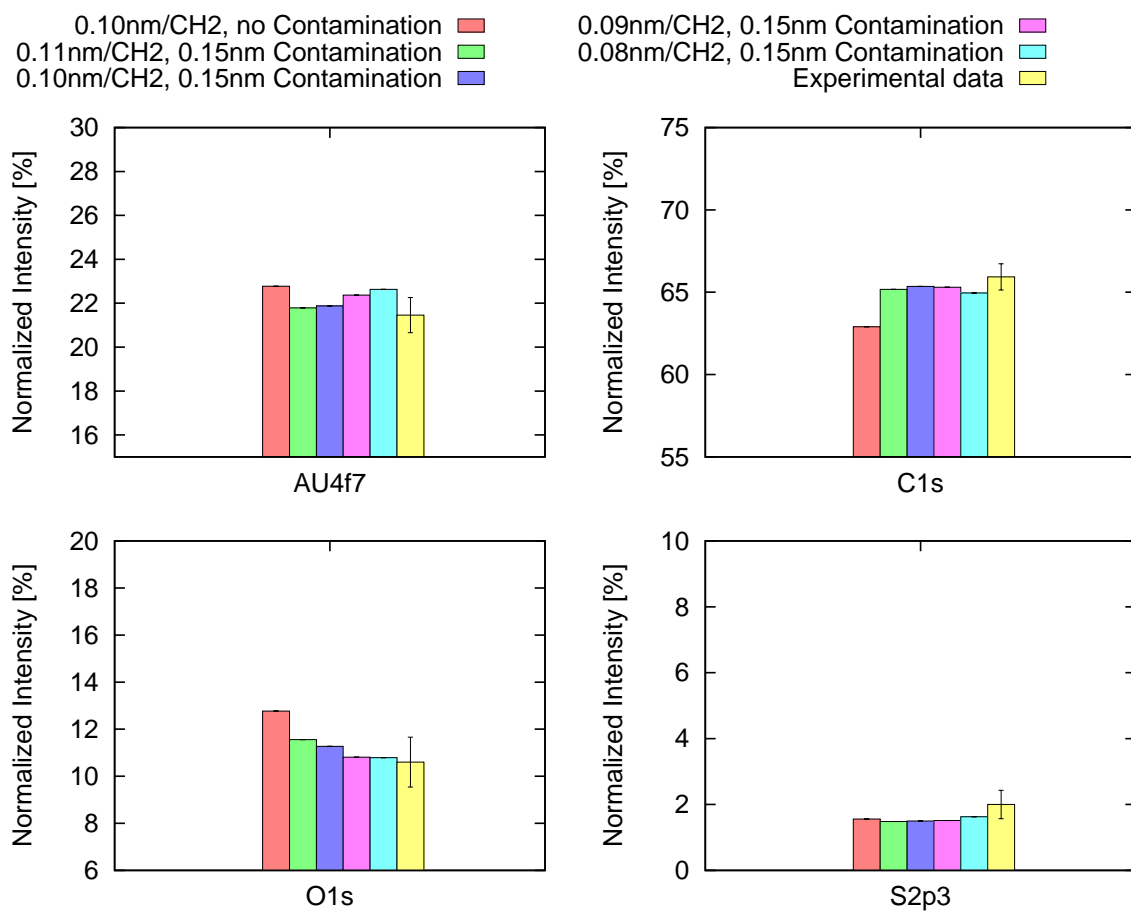
Figure III.9.: Comparison of normalized intensities of the C1s, Au4f, O1s and S2p peaks determined by XPS and simulations conducted for different CH_2 shell thicknesses and the presence and absence of a hydrocarbon surface contamination with SESSA 2.0

intensities of the C1s, Au4f, O1s and S2p photoelectron peaks are listed in table III.2 and compared with results obtained from SESSA 1.3 and SESSA 2.0 for an emission angle of 0° relative to the surface normal. To find the shell thickness with the best agreement between the experimentally determined atomic compositions $\%_{i,\text{Experiment}}$ and the simulated compositions $\%_{i,\text{SESSA}}$, the sum-of-squares difference, $\sum X^2$, shown in eq. (III.9) was calculated for each case:

$$\sum X^2 = \sum_{i=\text{Au,C,O,S}} \left(\%_{i,\text{SESSA}} - \%_{i,\text{Experiment}}\right)^2 \tag{III.9}$$

Figure III.10 shows the total value for the sum-of-squares difference $\sum X^2$ and the contributions to $\sum X^2$ from each element for each CH$_2$-thickness shown in figure III.9.

Based on this figure, it is clear that it is necessary to account for the CH$_2$ contamination layer to obtain results with satisfactory agreement with the experiment.
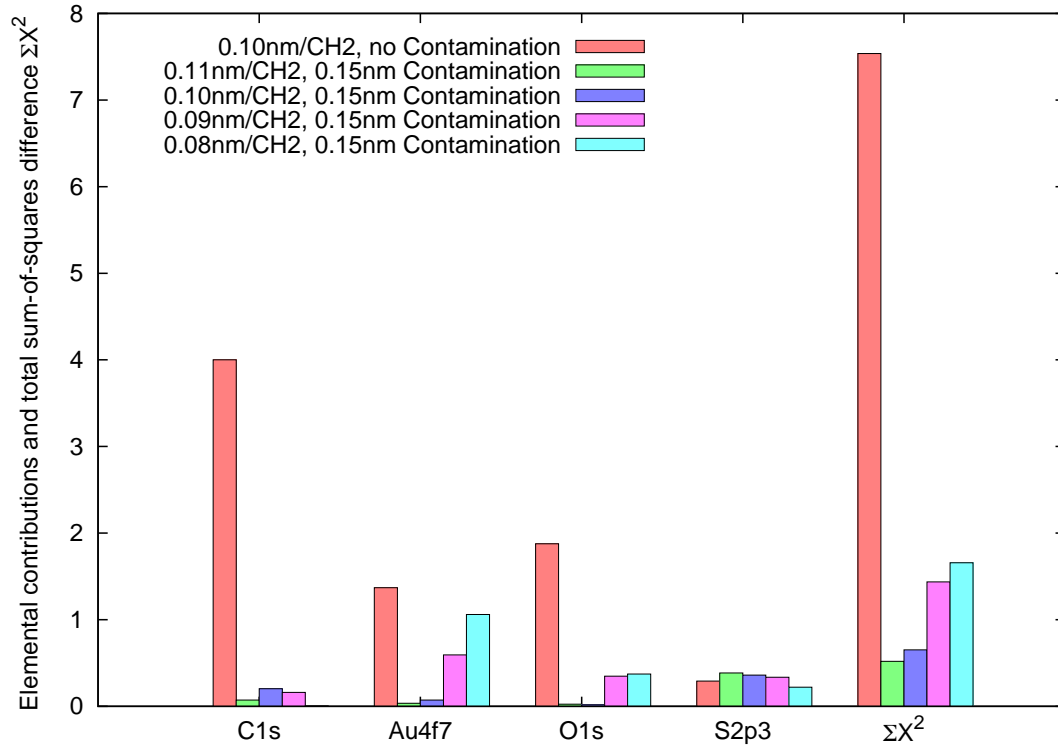

Figure III.10.: Contributions to the sum-of-squares difference for each case depicted in figure III.9 and the total sum-of-squares difference $\sum X^2$.

Compared with SESSA 1.3, the agreement with the experimental data for the carbon, gold and oxygen intensities is matched. The sulfur peak intensity simulated with SESSA 2.0, however, is slightly outside of the experimentally estimated standard deviation range. Based on the resulting sum-of-squares difference $\sum X^2$, displayed on the right side of figure III.10, the CH$_2$-thickness of 0.10 nm and 0.11 nm per CH$_2$-group and a

Table III.2.: Normalized intensities of the C1s, Au4f, O1s and S2p peaks determined by XPS measurements and simulations with SESSA 1.3 [15] and SESSA 2.0 with and without a surface hydrocarbon contamination layer for an emission angle of 0° relative to the surface normal

		Normalized intensities (%)		
PE line	Experiment	SESSA 1.3 with cont. layer 0.09 nm/CH_2 group	SESSA 2.0 with cont. layer 0.11 nm/CH_2 group	SESSA 2.0 without cont. layer 0.11 nm/CH_2 group
C1s	64.9 ± 1.1	64.7	65.2	62.9
Au4f	21.6 ± 0.4	21.5	21.8	22.8
O1s	11.4 ± 1.1	11.8	11.6	12.8
S2p	2.1 ± 0.3	1.9	1.5	1.6

hydrocarbon contamination layer of 0.15 nm give the best agreement with the experiment. This corresponds to a total film thickness of 2.00 nm and 2.15 nm, respectively, which is close to Techane's result of 1.85 nm.

4.3. Full spectal comparison between SESSA and experiment

With SESSA it is not only possible to simulate photoelectron peak intensities but also to simulate entire spectra. This feature of the software was used to conduct a full spectrum match between the measured and simulated spectra of the gold NP SAMs. The transmission function of the XPS apparatus used to record the spectra was estimated.

In contrast to all previously discussed cases where only the elastic (i.e. zero-loss) peak intensities were of interest, the inelastic background also needs to be correctly accounted for. As shown in a previous work [37], a single NP is a useful model system for dispersed powders and yields the same elastic-peak intensities. However, the inelastic background obtained from a single NP is significantly different from the inelastic background of a dispersed powder, and a more suitable morphology is needed to reproduce it correctly. Therefore, using external software a PENGEOM geometry of an array of dispersed CS particles resembling a powder was created and simulated with SESSA to ensure the correct shape of the inelastic background. However, SESSA assumes a constant transmission function, so in order to compare the experimental and simulated spectra with each other, a transmission-function correction needs to be applied to the experimental data. The transmission function was estimated as follows: First, the normalized intensities of the C1s, O1s and Au4f peaks were determined using the experimental spectra [15]. Then, each atomic composition was normalized to the Au4f peak and divided by the transmission-corrected data provided by Techane *et al.* in the original paper [15]. The sulfur peak was omitted and corrected for since the provided data did not allow us to extract useful data for the minor sulfur peaks. Plotting these elemental ratios for each element gives three points that represent a crude approximation for the transmission function normalized to the $Au4f_{7/2}$ binding energy of 84.0 eV. In order to validate this

result, a second approach was adopted where the experimental and the simulated spectra were divided by one another, followed by fitting a second-order polynomial through the ratio data. The derived function is a crude approximation for the transmission function, given that the differences between the experimental and simulated spectra are most likely due to the energy dependence of the transmission function.

Figure III.11a shows the simulated and experimental spectra, where the simulation was normalized to the C1s peak of the experiment. When comparing these spectra the simulated spectrum appears to be skewed relative to the experimental spectrum. This skewness can be partially attributed to the transmission function of the XPS instrument used for the experiment.

Correcting the experimental spectrum for the transmission function yields the spectrum shown in figure III.11b, which exhibits a nearly ideal agreement with the simulation. Also, as seen in figure III.11c, the transmission function obtained by comparing the atomic compositions as well as simply dividing one spectrum by the another yields very similar results.

Having an approximate expression for the transmission makes it possible to directly compare the experimental and simulated spectra. Figure III.12 shows experimental spectra for SAMs on gold NPs, and SAMs on flat gold, and the corresponding simulated spectra, all normalized to the Au4f peaks. For comparison a simulated spectrum of a single gold NP is displayed which exhibits a clearly different background shape.

The transmission-function correction was essentially derived using the experimental data for gold NPs and the corresponding simulation of a powder-like geometry. The same transmission correction was applied to the experimental spectrum for SAMs on flat gold, again leading to good agreement with the simulation. In general, it can be seen that the background shapes are distinguishable and that SESSA V2.0 is capable of correctly reproducing the background shape using an externally loaded PENGEOM geometry file, in contrast to the single-particle model, where only the peak-intensity ratios are correctly reproduced.

5. Summary and Conclusions

We have substantially improved SESSA by implementing the PENGEOM package that enables one to simulate different predefined nanomorphologies in addition to the previous functionality to simulate planar samples. Using the $T(NP)$ formula, a comparison of simulated and calculated shell thicknesses of CS NPs was made. The results obtained with SESSA 2.0 are in perfect agreement with the $T(NP)$ formula within the limits of the underlying model which is based on the SLA. With SESSA 2.0, it was very easy to study the limits of the $T(NP)$ formula and it was shown that it is highly suitable for determining shell thicknesses of organic materials but overestimates shell thicknesses for CS particles with strongly scattering shells.

Also, a number of differently aligned structures of core-shell particles was analyzed. It was shown that with increasing periodicity of the arrangements features in the angle-resolved spectra of the photoelectron intensitry ratio of the core and shell materials arise.
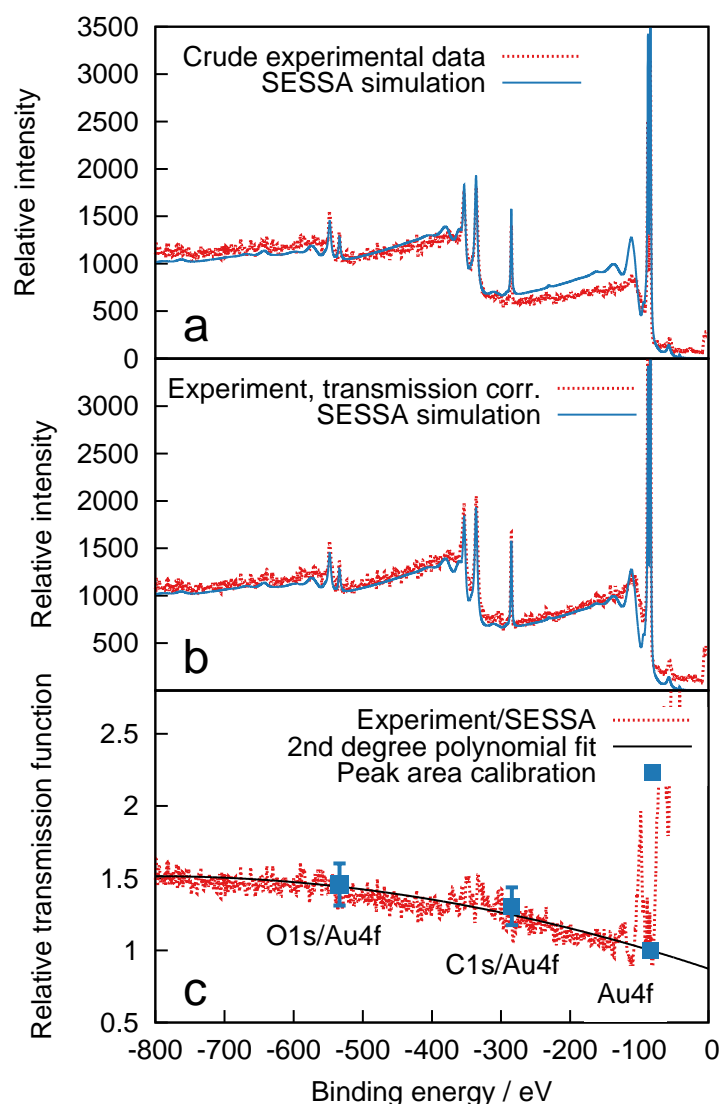
Figure III.11.: Experimental, simulated and transmission-corrected spectra of $C_{16}COOH$ SAMs on 14 nm gold NPs at an emission angle of 0° relative to the surface normal and the resultant approximation of the transmission function. **(a)** Comparison of experimental and simulated spectra, both normalized to the C1s peak. Since SESSA does not account for the transmission function of the experimental setup, the spectra do not match. **(b)** Comparison of the transmission-corrected experimental spectrum and the simulated spectrum. By fitting a second-degree polynomial to the transmission function and dividing the experimental spectrum by this function, very good agreement is obtained with the experimental spectum. **(c)** Display of the transmission function obtained by comparing elemental compositions together with the second-order polynomial fit for the binding-energy range between $-800\,\text{eV}$ and $-150\,\text{eV}$ and by dividing the experimental spectrum by the simulated spectum
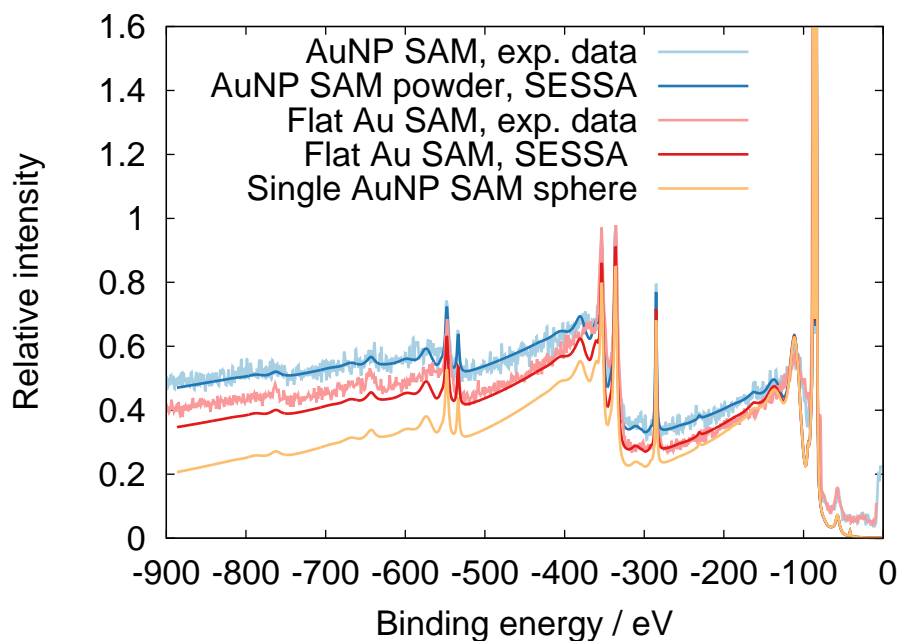
Figure III.12.: Comparison of transmission-corrected, experimental data for SAMs on flat gold and SAMs on gold NPs with the corresponding simulations. Also, the simulated spectrum of a single gold NP is shown. The clear difference in background shapes between the flat geometry and the NP is apparent. In contrast, the single gold NP model correctly predicts the peak-intensity ratio but exhibits a significantly different background shape.

Also, the validity of the single-sphere assumption was studied and it was shown that the intensity ratio of a core-shell particles is equivalent to the intensity ratio of a bulk powder.

SESSA 2.0 was also applied to a further analysis of experimental data (14 nm gold particles functionalized with an alkanethiol [15]) in which results were previously obtained with SESSA 1.3 and a model in which spherical particles were represented by an array of differently angled surfaces. With the new version of SESSA it was straightforward to allow the radial density to vary. For the total alkanethiol film thickness two values of 2.00 nm and 2.15 nm were found, which both gave equally good agreement with the experimental data, compared to the previous result of 1.85 nm [15].

Furthermore, we have compared experimental spectra for SAMs on flat gold and SAMs on 14 nm gold NP [15] with simulations. In order to compare experimental spectra with simulations, it was necessary to correct the simulations for the transmission function of the XPS instrument used to measure the experimental spectra. The corrected simulations exhibited very good agreement with the experimental spectra with regard to the shape of the inelastic background, thus showing that SESSA 2.0 is capable of correctly reproducing not only XPS peak intensities but also XPS spectra of dispersed arrays of CS particles. The spectra for SAMs on flat gold and gold NPs were then compared with the spectrum of

a single SAM gold NP, which is a model system often employed in XPS. This comparison was conducted to show the significant differences in the shape of the inelastic background that arise due to the presence of a dispersed array of NPs and which are missing if a single particle is simlated.

Bibliography

[1] C. J. Powell. Growth and trends in Auger-electron spectroscopy and x-ray photo-electron spectroscopy for surface analysis. *J. Vac. Sci. Technol. A*, 21(5):S42–S53, 2003.

[2] AI Ekimov, AL Efros, and AA Onushchenko. Quantum size effect in semiconductor microcrystals. *Solid State Commun.*, 1985.

[3] D.R. Baer, J.E. Amonette, M.H. Engelhard, D.J. Gaspar, A.S. Karakoti, S. Kuchibhatla, P. Nachimuthu, J.T. Nurmi, Y. Qiang, V. Sarathy, et al. Characterization challenges for nanomaterials. *Surface and Interface Analysis*, 40(3-4):529–537, 2008.

[4] Rob Phillips and Stephen R. Quake. The Biological Frontier of Physics, May 2006.

[5] Brooke T Mossman and Andrew Churg. Mechanisms in the pathogenesis of asbestosis and silicosis. *American journal of respiratory and critical care medicine*, 157(5):1666–1680, 1998.

[6] John D Aiken and Richard G Finke. A review of modern transition-metal nanoclusters: their synthesis, characterization, and applications in catalysis. *Journal of molecular catalysis A: chemical*, 145(1):1–44, 1999.

[7] EK Richman and JE Hutchison. The nanomaterial characterization bottleneck. *ACS Nano*, 2009.

[8] A.G. Shard. A straightforward method for interpreting XPS data from core-shell nanoparticles. *Journal of Physical Chemistry C: Nanomaterials and interfaces*, 116(31):16806–16813, 2012.

[9] W. Smekal, W.S.M. Werner, and C.J. Powell. Simulation of electron spectra for surface analysis (SESSA): a novel software tool for quantitative auger-electron spectroscopy and X-ray photoelectron spectroscopy. *Surface and Interface Analysis*, 37(11):1059–1067, 2005.

[10] W.S.M. Werner, W. Smekal, and C.J. Powell. NIST database for the simulation of electron spectra for surface analysis, version 2.0. `http://www.nist.gov/srd/nist100.cfm`, 2014.

[11] S Tougaard. Quases: Software package for quantitative xps. *AES of surface nanostructures by inelastic peak shape analysis*, 1994.

[12] W H Gries and W S M Werner. Take-off angle and film thickness dependence of the attenuation length of X-ray photoelectrons by a trajectory reversal method. *Surf. Interface Anal.*, 16:149, 1990.

[13] Herbert Kroemer. Nobel lecture: quasielectric fields and band offsets: teaching electrons new tricks. *Reviews of modern physics*, 73(3):783–793, 2001.

[14] F. Salvat-Pujol. *Secondary-electron emission from solids: Coincidence experiments and dielectric formalism*. PhD thesis, Vienna Universisity of Technology, 2012.

[15] S. Techane, D.R. Baer, and D.G. Castner. Simulation and modeling of self-assembled monolayers of carboxylic acid thiols on flat and nanoparticle gold surfaces. *Anal. Chem.*, 83(17):6704–12, September 2011.

[16] K. Siegbahn and C. Nordling. ESCA, atomic, molecular and solid state structure studied by means of electron spectroscopy. *Nov. Act. Uppsaliensis*, 1967.

[17] J.F. Watts and J. Wolstenholme. *An Introduction to Surface Analysis by XPS and AES*. John Wiley & Sons, Ltd, 2005.

[18] Martin Henzler and Wolfgang Göpel. *Oberflächenphysik des Festkörpers*. Vieweg Teubner Verlag, 1991.

[19] Wolfgang SM Werner. Electron transport for spectrum analysis and experiment design. *Journal of Electron Spectroscopy and Related Phenomena*, 178:154–177, 2010.

[20] CJ Powell and A Jablonski. The nist electron effective-attenuation-length database. *Journal of Surface Analysis*, 9(3):322–325, 2002.

[21] C.R. Brundle, G. Conti, and P. Mack. XPS and angle resolved XPS, in the semiconductor industry: Characterization and metrology control of ultra-thin films. *Journal of Electron Spectroscopy and Related Phenomena*, 178-179:433–448, May 2010.

[22] Aleksander Jablonski. Elastic scattering and quantification in aes and xps. *Surface and Interface Analysis*, 14(11):659–685, 1989.

[23] MP Seah and R White. Ultrathin SiO2 on Si: Iii mapping the layer thickness efficiently by xps. *Surface and interface analysis*, 33(12):960–963, 2002.

[24] OA Baschenko, GV Machavariani, and VI Nefedov. New technique for investigation of angular distribution of photoemission from solids. demonstration of the effect of elastic scattering. *Journal of electron spectroscopy and related phenomena*, 34(3):305–308, 1984.

[25] S Tougaard. Surface nanostructure determination by x-ray photoemission spectroscopy peak shape analysis. *Journal of Vacuum Science & Technology A*, 14(3):1415–1423, 1996.

[26] S. Tougaard. Energy loss in XPS: Fundamental processes and applications for quantification, non-destructive depth profiling and 3D imaging. *Journal of Electron Spectroscopy and Related Phenomena*, 178-–179(0):128–153, 2010. Trends in X-ray Photoelectron Spectroscopy of solids (theory, techniques and applications).

[27] Sven Tougaard. Energy loss in xps: Fundamental processes and applications for quantification, non-destructive depth profiling and 3d imaging. *Journal of Electron Spectroscopy and Related Phenomena*, 178:128–153, 2010.

[28] Sven Tougaard and Peter Sigmund. Influence of elastic and inelastic scattering on energy spectra of electrons emitted from solids. *Physical Review B*, 25(7):4452, 1982.

[29] S Tougaard and A Ignatiev. Concentration depth profiles by xps; a new approach. *Surface Science*, 129(2):355–365, 1983.

[30] S Tougaard. Composition depth information from the inelastic background signal in xps. *Surface Science*, 162(1):875–885, 1985.

[31] Sven Tougaard. Quantitative analysis of the inelastic background in surface electron spectroscopy. *Surface and Interface Analysis*, 11(9):453–472, 1988.

[32] S Tougaard et al. Accuracy of the non-destructive surface nanostructure quantification technique based on analysis of the xps or aes peak shape. *Surface and Interface Analysis*, 26(4):249–269, 1998.

[33] R Van Hardeveld and F Hartog. The statistics of surface atoms and surface sites on metal crystals. *Surface Science*, 15(2):189–230, 1969.

[34] Lev Davidovich Landau, JS Bell, MJ Kearsley, LP Pitaevskii, EM Lifshitz, and JB Sykes. *Electrodynamics of continuous media*, volume 8. elsevier, 1984.

[35] W.H. Gries and W.S.M Werner. Take-off angle and film thickness dependences of the attenuation length of X-ray photoelectrons by a trajectory reversal method. *Surface and Interface Analysis*, 16(1-12):149–153, 1990.

[36] F. Salvat, J.M. Fernández-Varea, and J. Sempau. PENELOPE-2006: A code system for Monte Carlo simulation of electron and photon transport. In *Workshop Proceedings*, volume 4, page 7, 2006.

[37] W.S.M. Werner, M. Chudzicki, W. Smekal, and C.J. Powell. Interpretation of nanoparticle X-ray photoelectron intensities. *Applied Physics Letters*, 104(24):243106, 2014.

[38] A. Frydman, D.G. Castner, M. Schmal, and C.T. Campbell. Particle and phase thicknesses from XPS analysis of supported bimetallic catalysts: Calcined Co-Rh/Nb_2O_5. *Journal of Catalysis*, 152(1):164–178, 1995.

[39] D.R. Baer and M.H. Engelhard. XPS analysis of nanostructured materials and biological surfaces. *Journal of Electron Spectroscopy and Related Phenomena*, 178-179:415–432, 2010.

[40] A.N. Shipway, E. Katz, and I. Willner. Nanoparticle arrays on surfaces for electronic, optical, and sensor applications. *ChemPhysChem*, 1(1):18–52, 2000.

[41] Q.A. Pankhurst, J. Connolly, S.K. Jones, and J. Dobson. Applications of magnetic nanoparticles in biomedicine. *Journal of Physics D: Applied Physics*, 36(13):R167–R181, July 2003.

[42] C.J. Murphy, T.K. Sau, A.M. Gole, C.J. Orendorff, J. Gao, L. Gou, S.E. Hunyadi, and T. Li. Anisotropic metal nanoparticles: Synthesis, assembly, and optical applications. *Journal of Physical Chemistry B*, 109(29):13857–70, July 2005.

[43] R. Thakar, Y. Chen, and P. Snee. Efficient emission from core/(doped) shell nanoparticles: applications for chemical sensing. *Nano Letters*, 7(11):3429–32, 2007.

[44] W.H. De Jong and P.J.A. Borm. Drug delivery and nanoparticles: applications and hazards. *International Journal of Nanomedicine*, 3(2):133–49, 2008.

[45] C.J. Powell and A. Jablonski. Surface sensitivity of X-ray photoelectron spectroscopy. *Nuclear Instruments and Methods in Physics Research Section A: Accelerators, Spectrometers, Detectors and Associated Equipment*, 601(1):54–65, 2009.

[46] C.J. Powell and A. Jablonski. Progress in quantitative surface analysis by X-ray photoelectron spectroscopy: Current status and perspectives. *Journal of Electron Spectroscopy and Related Phenomena*, 178-179:331–346, May 2010.

[47] H.A. Biebuyck, C.D. Bain, and G.M. Whitesides. Comparison of organic monolayers on polycrystalline gold spontaneously assembled from solutions containing dialkyl disulfides or alkanethiols. *Langmuir*, 10(6):1825–1831, 1994.

[48] H.S. Hansen, S. Tougaard, and H. Biebuyck. The adsorption of alkanethiols on gold studied quantitatively by XPS inelastic background analysis. *Journal of Electron Spectroscopy and Related Phenomena*, 58(1-2):141–158, 1992.

[49] J.P. Folkers, P.E. Laibinis, and G.M. Whitesides. Self-assembled monolayers of alkanethiols on gold: comparisons of monolayers containing mixtures of short-and long-chain constituents with methyl and hydroxymethyl terminal groups. *Langmuir*, 8(5):1330–1341, 1992.

[50] W.D. Luedtke and U. Landman. Structure and thermodynamics of self-assembled monolayers on gold nanocrystallites. *Journal of Physical Chemistry B*, 102(34):6566–6572, 1998.

[51] J. C. Love, L.A. Estroff, J.K. Kriebel, R.G. Nuzzo, and G.M. Whitesides. Self-assembled monolayers of thiolates on metals as a form of nanotechnology. *Chemical Rewviews*, 105(4):1103–1170, 2005.

[52] M.-C. Daniel and D. Astruc. Gold nanoparticles: assembly, supramolecular chemistry, quantum-size-related properties, and applications toward biology, catalysis, and nanotechnology. *Chemical Rewviews*, 104(1):293–346, 2004.

[53] D.W. Grainger and D.G. Castner. Nanobiomaterials and nanoanalysis: opportunities for improving the science to benefit biomedical technologies. *Advanced Materials*, 20(5):867–877, 2008.

[54] R. Van Hardeveld and F. Hartog. The statistics of surface atoms and surface sites on metal crystals. *Surface Science*, 15(2):189–230, 1969.